

Experimental investigation of dynamic drying in single pharmaceutical granules containing acetaminophen or carbamazepine using synchrotron X-ray micro computed tomography

Carter Blocka ^a, Xiao Fan Ding ^b, Ning Zhu ^{a,b,c}, Lifeng Zhang ^{a,*}

^a Department of Chemical and Biological Engineering, University of Saskatchewan, Saskatoon, SK, Canada

^b Department of Biomedical Engineering, University of Saskatchewan, Saskatoon, SK, Canada

^c Canadian Light Source Inc., Saskatoon, SK, Canada

ARTICLE INFO

Keywords:

Pharmaceuticals
Synchrotron
X-ray imaging
Granular materials
Drying
Moisture content
Porosity

ABSTRACT

Drying time, velocity, and temperature are important aspects of the drying process for pharmaceutical granules observed during tablet manufacturing. However, the drying mechanism of single granules is often limited to modelling and simulation, with the internal and physical changes difficult to quantify at an experimental level. In this study, in-situ synchrotron-based X-ray imaging techniques were used for the first time to investigate the dynamic drying of single pharmaceutical granules, quantifying internal changes occurring over the drying time. Two commonly used excipients (lactose monohydrate (LMH) and microcrystalline cellulose (MCC)) were used as pure components and binary mixtures with one of either two active pharmaceutical ingredients of differing hydrophilicity/hydrophobicity (acetaminophen (APAP) and carbamazepine (CBZ)). Water was used as a liquid binder to generate single granules of 25 % to 30 % moisture content. Results showed that for most samples, the drying time and composition significantly influences the pore volume evolution and the moisture ratio, with the velocity and temperature of the drying air possessing mixed significance on increasing the rate of pore connectivity and moisture removal depending on the sample composition. Effects of active ingredient loading resulted in minimal influence on the drying of CBZ and generated binary mixtures, with APAP and its respective mixtures' drying behaviour dominated by the material's hydrophilic nature.

1. Introduction

Within the pharmaceutical tableting process, the drying of wet granules by a convective method is an essential unit operation in the preparation of the product for the downstream process of compaction and packaging. The removal of moisture is used to extend a product's shelf life, decreasing the weight of the product while simultaneously ensuring stability (Deck et al., 2022; Yadav and Kumar, 2014). For this application, fluidized bed drying is most commonly used, possessing a high level of mass and energy transfer that is observed between the drying gas and the individual granules (Salmon et al., 2007; Kan and H., & Watano, S., 2018). The drying kinetics within the initial stages of drying are governed by aspects of velocity, temperature, and humidity, with Fick's law describing the rate of liquid diffusion as proportional to the concentration gradient with consideration to the water vapour concentration at the surface (Lehmann et al., 2020; Maxwell, 1890).

Following the initial period, the falling rate period introduces more complex moisture removal, with the liquid surface receding and affecting surface tension in the granule formation (Breinlinger et al., 2015). Additionally, the intergranular pore network further allows for liquid transport to the vapour-liquid interface at the granule surface, with evaporation permitting the removal of moisture (Mezhericher et al., 2007; Mortier et al., 2012; Breinlinger et al., 2015; Vandepitte et al., 2024).

Well documented within the literature, key factors of drying air velocity and temperature influence the drying process by shortening the drying time as these parameters increase in value (Taghavivand et al., 2017; Putra and Ajiwiguna, 2017; Reyer et al., 2020; Zammouri et al., 2022). However, certain materials such as acetaminophen found within the pharmaceutical industry are susceptible to degradation at elevated temperatures while moisture is present (Gilpin and Zhou, 2004), limiting the conditions of the drying operation to maximize the drying rate while minimizing these undesirable effects. The addition of active

* Corresponding author.

E-mail address: lifeng.zhang@usask.ca (L. Zhang).

Nomenclature

| | |
|----------------------|---|
| A, B, C, D, E, F | Curve fitting parameters |
| C_p | Specific heat capacity |
| D_{eff} | Moisture diffusion coefficient |
| k | Thermal conductivity |
| MR | Moisture ratio |
| N/N_0 | Attenuation |
| r | Sample radius |
| t | Time |
| T | Temperature |
| l | Sample thickness |
| X | Moisture content |
| X_0 | Initial moisture content |
| X_{eq} | Equilibrium moisture content |
| <i>Greek symbols</i> | |
| ϵ | Porosity |
| μ | Linear attenuation coefficient |
| μ_a | Linear attenuation coefficient for air |
| μ_s | Linear attenuation coefficient for solids |
| μ_w | Linear attenuation coefficient for water |
| ρ | Density |

pharmaceutical ingredients into mixtures may also affect the final granules' characteristics, with size, shape, and density observed as influential parameters (Li et al., 2019; Asada et al., 2017). Furthermore, different types of pharmaceutical ingredients exhibit flowability challenges as mechanical properties change in the presence of moisture. While diluent and binder materials such as lactose monohydrate are observed to form a paste-like slurry at elevated moisture contents by dissolving directly into the water, active ingredients such as acetaminophen and carbamazepine form very hard solids, with other materials such as microcrystalline cellulose exhibiting mild yet loose clumping while still maintaining flowability due to the complex nature of water uptake (Blocka et al., 2023; Khoo et al., 2010). The differences in these mechanical properties and each material change in the presence of moisture are consequently important in determining the final granules attributes, and by proxy, tableted products. This is further justified for some of the most common excipients in the tablet manufacturing process, such as microcrystalline cellulose, whose interactions with water are complicated due to particles swelling and shrinking during the wetting and drying processes respectively (Kyttä et al., 2020).

The moisture content changes observed in the drying process have previously been documented alongside changes observed in the pore volume as significant parameters on the thermal conductivity and volumetric specific heat capacity for common pharmaceutical components and mixtures (Blocka et al., 2023). These thermal properties are of particular importance for granular materials of high sphericity, as various mathematical drying models evaluate thermal properties within the equations of mass and heat transfer in spherical coordinates (Mezhericher et al., 2007; Assar et al., 2016).

In investigating single granule materials and the drying operations surrounding them, limited research has been performed on an experimental level, with primary emphasis on the literature surrounding models and simulation (Breinlinger et al., 2015; Mezhericher et al., 2007; Mortier et al., 2012; Vandeputte et al., 2023). Previous works by Groenewold et al. (Groenewold et al., 2002) aimed to determine single-particle drying kinetics using acoustic levitation for $\gamma\text{-Al}_2\text{O}_3$. Experiments were conducted between 25 °C and 30 °C with air velocity varied between 0.020 m/s and 0.088 m/s, measuring outlet humidity using a hygrometer. The findings of this work were comparable to results observed in a drying channel or a microbalance, with accurate

derivations of drying curves feasible up to 0.065 m/s. This method presents an attractive experiment design that can be performed easily and quickly, with the entire surface area of the particles exposed to the drying air as intrusive support is not required. However, the particles are subject to the primary effects of acoustic streaming, producing a higher drying rate than expected by the boundary layer theory (Schiffter and Lee, 2007). In addition to this, the particles tend to move around, making the positioning and tracking of the particles difficult. Another study by Janocha and Tsotsas (Janocha and Tsotsas, 2022) examined single sessile droplets drying using a cuboid glass drying chamber with laminar flow. Experiments were conducted between 21 °C and 75 °C, with air velocity varied between 0.1 m/s and 1.5 m/s. The methodology of the experiment used X-ray micro-computed tomography to gain information on the inner structure of the samples during the drying process. The methods within this work present an attractive option for visualizing the drying process using X-ray micro-computed tomography, with the ease of use in positioning a single, stationary sample within a relatively simple apparatus that can be connected to an existing, preconditioned air stream. However, the samples must have the downside of being fixed to a substrate to eliminate motion artifacts during imaging (Rantalainen et al., 2018), not allowing for the entire surface area of the sample to be exposed to the drying air.

While the studies of single granule drying are limited due to concerns of fast drying kinetics and instability during imaging brought upon by sample motion, several investigations using synchrotron X-ray micro-computed tomography have previously been conducted for pharmaceuticals on a dynamic scale. Lab-based micro-computed tomography is highly time-consuming for obtaining a high-resolution dataset, with dynamic studies not being feasible as imaging times can take up to a few hours within a limited field of view of the sample (Keklikoglou et al., 2021). Due to lab-based limitations and the time required to obtain high-resolution data, it can be expected that any changes occurring within a sample during imaging can lead to multiple artifacts that can make analysis too involved or the data unusable (Triche et al., 2019; Barrett and Keat, 2004). Conversely, synchrotron-based X-ray imaging can overcome the challenges seen in conventional methods. Possessing a high flux with good stability, synchrotron X-ray micro-computed tomography can obtain high contrast results much faster than conventional methods, with single high-resolution scans taking a matter of seconds, in addition to much greater spatial and temporal resolutions (Danalou et al., 2022).

Synchrotron imaging has been used to capture rapidly occurring processes, emphasizing the use of X-ray projections and micro-computed tomography. In works by Li et al. (Li et al., 2019; Li et al., 2021), common pharmaceutical powders were quantitatively studied using a single droplet impact method to study the dynamic wet granulation process using synchrotron-based X-ray imaging techniques. These works found that the particle properties of size, sphericity, and hydrophilicity significantly influence the granulation process and the resulting granules, with the internal structure differences and porosity of each granule decreasing from the top of the granule to the bottom (Li et al., 2019). Furthermore, these studies demonstrated a high potential for applying synchrotron X-ray imaging for studying dynamic processes, with further experiments drawing more information for single droplet studies that analyzed spreading and tunnelling mechanisms within pharmaceutical materials, better-describing water movement and penetration (Li et al., 2021). In works by Danalou et al. (Danalou et al., 2022; Zeinali Danalou et al., 2023), synchrotron-based X-ray imaging techniques were once again applied, visualizing the real-time wetting process of pharmaceutical powder beds for various binary mixtures and liquid binders. These works found that for most compositions, an increase in porosity is observed for higher active pharmaceutical ingredient loading in the form of acetaminophen, with further results showing significant differences in agglomeration depending on the excipient used and the selected liquid binder (Danalou et al., 2022). Additionally, a single droplet impact method was implemented to evaluate the rate of pore evolution

and distribution during the dynamic wetting process, further demonstrating the effectiveness and attractiveness of using synchrotron-based X-ray imaging methods for complex and fast processes that occur within opaque materials such as pharmaceuticals (Zeinali Danalou et al., 2023).

Therefore, the objectives of this study were (a) to investigate and compare the single granule drying behaviour of acetaminophen (APAP), microcrystalline cellulose (MCC), lactose monohydrate (LMH), and carbamazepine (CBZ) for pure components and binary mixtures under several drying air velocities and temperatures, and (b) to visualize and quantify the changes for single granules undergoing the drying process with the aid of synchrotron X-ray applications to characterize the 3D internal properties with emphasis on changes within the pore volume and changes in the moisture content of a sample. This work aimed to study the real-time single-granule drying dynamics for various individual pharmaceuticals and mixtures.

2. Theory and modelling

The modelling of single particle and single granular drying are derived in spherical geometries for simplicity and convenience in numerical analysis, with results often comparable in accuracy to more complex geometries (Prakash and Pan, 2012). Equations of heat and mass transfer in a sphere can be represented by taking into consideration Fourier's law of heat conduction and Fick's law of diffusion respectively. These are presented by the following equations:

$$\frac{dX}{dt} = \frac{1}{r^2} \frac{\partial}{\partial r} (r^2 D_{eff} \frac{\partial X}{\partial r}) \quad (1)$$

$$\frac{\partial(\rho C_p T)}{\partial t} = \frac{1}{r^2} \frac{\partial}{\partial r} (r^2 k \frac{\partial(T)}{\partial r}) \quad (2)$$

where X is the moisture content of the granule; t is time; D_{eff} is the moisture diffusion coefficient; r is the radius of the granule; ρ is the granule density; C_p is the specific heat capacity; T is the temperature; k is the thermal conductivity.

In the drying model, with emphasis on the equation for heat transfer, the parameters of specific heat capacity and thermal conductivity can be seen. In previous works, these parameters have been determined to be significantly impacted by the moisture content and porosity of a given material (Blocka et al., 2023), complicating the solutions to these equations as they must be solved simultaneously. These thermal properties can be predicted by the following equations:

$$k = (A^*(1-X) + B^*X)(1-\varepsilon) + C^*\varepsilon \quad (3)$$

$$\rho C_p = (D^*(1-X) + E^*X)(1-\varepsilon) + F^*\varepsilon \quad (4)$$

where A, B, C, D, E, and F are curve fitting parameters; k is the thermal conductivity; ρC_p is the volumetric specific heat capacity; X is the moisture content of the sample; ε is porosity.

However, during the drying process, the removal of moisture and the evolution of pore volume changes can be observed throughout the process, giving way to a time dependency for the parameters of moisture content (X) and the contribution of air to the porosity (ε). These parameters are therefore important to monitor during the drying of singular granular media, as more refined modelling can be produced to better predict a material's drying endpoint.

In predicting moisture content changes for a given period, several popular models found within the literature can be used to predict the moisture ratio as a function of time such that all obtained results of a study are comparable (Li et al., 2022; He et al., 2021). The moisture ratio can be described as:

$$MR = \frac{X - X_{eq}}{X_0 - X_{eq}} \quad (5)$$

where MR is the moisture ratio; X is the moisture content; X_0 is the initial

moisture content; X_{eq} is the equilibrium moisture content. However, the equilibrium moisture content is often negligible (Celma et al., 2012; Sacilik and Elicin, 2006), and a simplified approximation can be used in the form:

$$MR = \frac{X}{X_0} \quad (6)$$

where MR is the moisture ratio; X is the moisture content; X_0 is the initial moisture content.

3. Materials and methods

3.1. Materials

Four pharmaceutical powders were investigated in this study, with reverse osmosis water used as a liquid binder. Two common excipients were selected for comparison between drying behaviour and the effect of active pharmaceutical ingredient loading. Two active pharmaceutical ingredients were chosen to examine the effect of hydrophobicity on the drying. The physical characteristics of each pharmaceutical powder can be seen in Table 1. The model drugs of acetaminophen and carbamazepine were selected due to their diverse physical properties. Acetaminophen has been shown to be a relatively hydrophilic material with moderate stability, whose influence on the drying process is well-understood within the literature. Carbamazepine has been shown to be moderately hydrophobic, whose poor solubility profile serves to contrast the moderate solubility associated with acetaminophen. In addition, both acetaminophen and carbamazepine are widely used in clinical settings, relevant for studies that aim to optimize processes within the tabletting industry, such as drying for commonly used medications.

The initial moisture content of individual samples and mixtures was brought to 30 % w/w, except for pure lactose monohydrate at 25 % w/w. The moisture content of each sample was measured using an HC103 Halogen Moisture Analyzer (METTLER TOLEDO, Canada). Granules of 3.29 ± 0.45 mm were used, similar to those sizes seen in a previous study (Zeinali Danalou et al., 2023). Characterization of APAP, MCC, and LMH was previously performed by Danalou (Danalou et al., 2022; Zeinali Danalou et al., 2023).

The pharmaceutical powders used in this study are often abbreviated based on their composition. To clarify the naming and present the mass percentages of each powder, Table 2 presents the naming of each sample in addition to their composition and granule diameters.

Table 1
Properties of pharmaceutical powders.

| Component | Abbreviation | Median particle size, d_{50} (μm) | Particle skeletal density, ρ_p (g/cm^3) | Supplier |
|-------------------------------|-----------------------|--|--|-----------------------------|
| Danalou et al., 2022; | Danalou et al., 2022; | | | |
| Zeinali Danalou et al., 2023) | Danalou et al., 2023) | | | |
| Acetaminophen | APAP | 50.9 ± 3.9 | 1.701 ± 0.001 | Hebei Jiheng Pharmaceutical |
| Carbamazepine | CBZ | 37.4 ± 12.5 | 1.381 ± 0.001 | Sigma-Aldrich |
| Microcrystalline Cellulose | MCC | 110.4 ± 6.6 | 1.555 ± 0.009 | FMC BioPolymers |
| Lactose Monohydrate | LMH | 47.9 ± 2.3 | 1.543 ± 0.004 | Foremost Farms |

Table 2
Labeling of pharmaceutical powders used in this study.

| Sample Name | Composition (mass percentage) | Wet Granule Projected Area Diameter (mm) | Dry Granule Projected Area Diameter (mm) | Change in Projected Area Diameter (mm) |
|-------------|--|---|---|--|
| APAP | 100 % Acetaminophen | 3.36 ± 0.33 | 3.36 ± 0.33 | 0.00 ± 0.00 |
| | | | | |
| CBZ | 100 % Carbamazepine | 3.48 ± 0.37 | 3.43 ± 0.34 | 0.05 ± 0.07 |
| | | | | |
| MCC | 100 % Microcrystalline Cellulose | 3.27 ± 0.34 | 3.11 ± 0.35 | 0.15 ± 0.02 |
| | | | | |
| LMH | 100 % Lactose Monohydrate | 3.23 ± 0.40 | 3.23 ± 0.40 | 0.00 ± 0.00 |
| | | | | |
| 90MCC10APAP | 90 % Microcrystalline Cellulose 10 % Acetaminophen | 3.42 ± 0.27 | 3.25 ± 0.28 | 0.18 ± 0.07 |
| | | | | |
| 80MCC20APAP | 80 % Microcrystalline Cellulose 20 % Acetaminophen | 3.23 ± 0.50 | 3.10 ± 0.49 | 0.12 ± 0.03 |
| | | | | |
| 50MCC50APAP | 50 % Microcrystalline Cellulose 50 % Acetaminophen | 3.29 ± 0.13 | 3.27 ± 0.08 | 0.02 ± 0.09 |
| | | | | |
| 90LMH10APAP | 90 % Lactose Monohydrate 10 % Acetaminophen | 3.66 ± 0.20 | 3.66 ± 0.20 | 0.00 ± 0.00 |
| | | | | |
| 80LMH20APAP | 80 % Lactose Monohydrate 20 % Acetaminophen | 3.22 ± 0.15 | 3.22 ± 0.15 | 0.00 ± 0.00 |
| | | | | |
| 50LMH50APAP | 50 % Lactose Monohydrate 50 % Acetaminophen | 3.41 ± 0.33 | 3.41 ± 0.33 | 0.00 ± 0.00 |
| | | | | |
| 50MCC50CBZ | 50 % Microcrystalline Cellulose 50 % Carbamazepine | 3.53 ± 0.35 | 3.45 ± 0.31 | 0.09 ± 0.06 |
| | | | | |
| 50LMH50CBZ | 50 % Lactose Monohydrate 50 % Carbamazepine | 3.24 ± 0.15 | 3.24 ± 0.15 | 0.00 ± 0.00 |
| | | | | |

3.2. Equipment

The pharmaceutical samples were positioned onto a custom-designed support made from 3D-printed polylactic acid (PLA) (Fig. 1b)). The design of the support is that of three cylinders at an offset angle, allowing for various morphological differences between granules to be permitted into the sample holder.

While methods of fluidization or acoustic levitation would be ideal in exposing the entirety of the samples to the drying air, the movement of the samples observed within these methods would lead to motion artifacts even with fast scan times of a matter of seconds at synchrotron facilities. Furthermore, it is expected that the positioning of the sample would be different between scans, making data analysis very difficult as certain regions of interest would be found in different locations if a scan were feasible with those methods. Therefore, support is necessary to attempt to expose the sample to the drying air as much as possible, while minimizing surface area that would be covered by a substrate.

The 3D-printed support is inserted into a polyetheretherketone (PEEK) vessel that is sealed by a lid and flange to allow the body of the vessel to rotate during scans. PEEK was selected as the construction material for the vessel due to its high durability and low x-ray absorption rate (Zhang et al., 2021). The PEEK vessel can be seen in Fig. 1a).

To monitor parameters of temperature and relative humidity, sensors

are positioned at the inlet, outlet, and within the vessel, with measurements sent to an external data logging system to monitor parameters of temperature and relative humidity throughout the experiments.

Connected to the inlet of the PEEK vessel is an air pre-conditioning setup. Building air is fed into the setup at 100 psi and ambient temperatures (23 °C), proceeding through a heater that is connected to a PID controller, with a temperature probe positioned after a needle valve to maintain the desired temperature. The air then proceeds through a flow meter to ensure the desired air flow rate going to the vessel and then travels through a length of flexible tubing that then connects to the PEEK vessel. The region after the needle valve is covered in a heated blanket to maintain temperature, and the entire main section is covered in insulation to reduce thermal losses. The flexible tubing is attached to a length of heat tape that is connected to its manual controller to further maintain temperature and is wrapped in insulating heat wrap. The length of tubing and the heating associated was to remain flexible as the piping had to be oriented in such a way that the connections to the PEEK vessel would stay outside of the region of the beam at the Canadian Light Source and still allowed for some rotation while connected to the CT rotation stage. A diagram of the entire setup can be seen in Fig. 2.

Interval CT scans of *in situ* single granule drying were performed over the drying time at the 05B1-1 beamline of the Biomedical Imaging and Therapy Facility (BMIT) at the Canadian Light Source (CLS). The X-ray source was a filtered white beam that was filtered through a 0.8 mm aluminum filter, with a peak photon energy of 20 keV at a current of 220 mA. X-ray projections were captured through an indirect detection optical system composing of an AA-40 beam monitor (Hamamatsu Photonics K.K., Japan) attached to a 500 μm-thick LuAG scintillator coupling with a PCO.DIMAX HS4 camera (PCO AG, Germany). It has an effective pixel size of 5.5 μm. Additional experiments were also conducted where projections were captured by an indirect detector with a Whitebeam microscope (Optique Peter) with 2X magnification and a 200 μm thick LuAG scintillator coupling with a PCO.DIMAX HS4 camera (PCO AG, Germany). It has an effective pixel size of 6 μm. A sample-to-detector distance of 30 cm was selected to improve absorption and edge enhancement of the obtained data while minimizing the effects of coherent diffraction, without the sample-to-detector distance becoming too short such that the Compton scattering photons would increase and result in deteriorated spatial resolution (Seo et al., 2012).

Each raw CT dataset consisted of 10 scans taken over 25 min, determined to be the drying endpoint for all samples where relative humidity measurements at the vessel outlet would no longer change. Each dataset included 20 dark-field images and 50 flat-field images for flat-field image correction. The data acquisition speed for each scan was 1500 projections per 180° rotation of the sample, with no delay between projections at an exposure time of 1 ms. These scanning parameters were determined to be the most optimal. Adjustments could be made to the exposure time, although an increase would result in a slower temporal resolution that would compromise capturing dynamic processes, or a shorter exposure time that would result in a poorer signal-to-noise ratio (Ding et al., 2023). The field of view (FOV) for each projection was 8.14 mm × 3.56 mm.

3.3. Experimental procedure

The moisture content, X, was measured for each sample before each experiment using an HC103 Halogen Moisture Analyzer.

Samples were first prepared by measuring out a small amount of the unwetted powders into small plastic containers, with binary mixtures measured by a mass ratio. The samples were generated in a larger quantity using a high shear mixer, incorporating water to the desired moisture content over an extended period. For binary and wetted mixtures, the samples were mixed thoroughly for 5 min until a homogenous state was reached. The samples were then sieved through a 3.36 mm sieve, apart from pure LMH whose granules were formed by rolling a small amount of paste into a spherical shape using a micro spatula. The

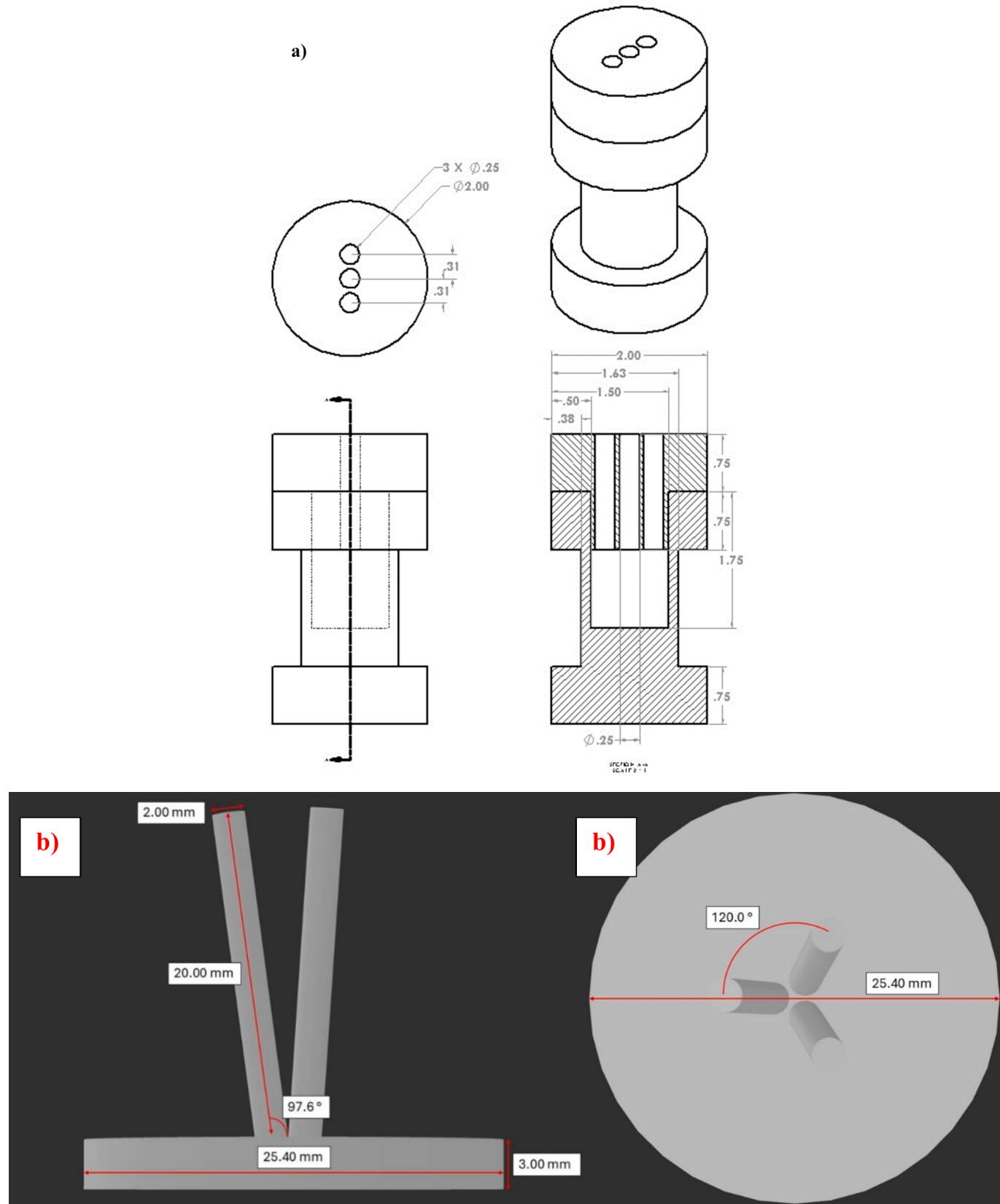


Fig. 1. a) Drawing of the PEEK Vessel used to contain individual granules and PLA support (dimensions in inches), b) Side and top-down view of 3D printed PLA support for single granules.

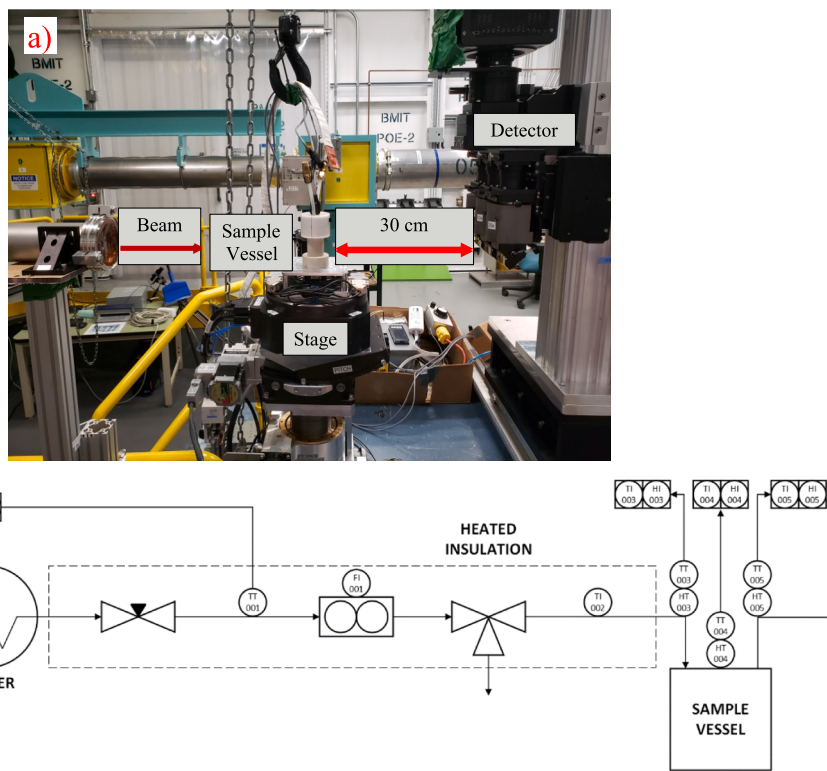


Fig. 2. a) In situ setup of single granule drying apparatus at 05B1-1 beamline, b) Process flow diagram of single granule drying apparatus.

moisture content of the samples was determined before each experiment, with reverse osmosis water added to the powders until the desired moisture content was achieved. Moisture content was determined using an HC103 Halogen Moisture Analyzer (METTLER TOLEDO, Canada). To allow for a uniform distribution within the bulk material, the wetted samples were allowed to rest for 15 min in an airtight container to reach equilibrium, similar to a previous study (Blocka et al., 2023). All samples were brought to 30 % moisture content, apart from pure LMH which was brought to 25 % moisture content as further increasing the addition of moisture would see the samples transform into a slurry. Samples were used immediately after preparation and were discarded if not currently in use. Each sample was disposed of at the end of each experiment. Multiple PLA supports were used such that previously used supports could be cleaned with reverse osmosis water and left to dry while at least one clean support could be used in the PEEK vessel. Single granules of approximately 3 mm in diameter (3.29 ± 0.45 mm observed from reconstructed CT data) that were spherical in nature were selected from the bulk and positioned on the PLA supports using a micro spatula before being inserted into the PEEK vessel and enclosed with the lid and flange. For each experiment, a single granule was used.

The PEEK vessel was screwed into the CT stage by an M4 screw, with the lid of the vessel connected to the air pre-conditioning setup adjacent to the stage. The length of flexible tubing and data acquisition cables were supported by an overhead crane to stay out of the way of the beam. Building air was connected to the system within the hutch, with manual valves used to vary the drying air velocity between 0.02 m/s and 0.10 m/s within the sample vessel as read by the flow meter. Heating elements were connected electrically to wall power and monitored by the individual controllers and the sensors connected to the PEEK vessel, with temperatures varying between 25 °C and 40 °C.

The drying air was permitted to reach steady state based on the output of the flow meter and the temperature sensors connected to the sample vessel and was maintained for five minutes before being redirected away from the sample vessel. The flanges fastening the lid of the vessel were removed to allow for a pre-prepared sample to be inserted

with the tripod support, affixing the supports to the base of the vessel using double sided tape. The vessel was then reassembled and an initial scan was taken of the sample before the drying air was directed to the sample vessel to begin the air drying process.

Scans were taken at intervals of 1 min for the first 5 min, and then every 5 min until 25 min had elapsed. At the rate of 1500 projections per CT scan, it was not possible to perform interval scanning faster than one minute as there is a buffer time between scans because of the data being saved from the RAM. Data acquisition was then stopped, the hutch was opened, and the sample was removed with the PLA support from the PEEK vessel. The PEEK vessel was put back together with a new, clean PLA support to maintain temperature. The sample was discarded, and the PLA support was cleaned with reverse osmosis water and set aside to dry while an already clean support was substituted in its place. The system was then reset for another experiment.

With the obtained raw data, CT reconstruction with phase retrieval was performed using UFO-KIT-based software (Farago et al., 2022; Vogelgesang et al., 2016). Dark and flat images were collected to spatially normalize the images where no sample was present. An example of the collected projections and the CT reconstruction process can be seen in Fig. 3.

Thresholding was performed using ImageJ (National Institutes of Health, USA) and Dragonfly version 2022.2.0.1367 (Objects Research Systems (ORS) Inc., Canada) was used for 3D rendering and to measure regions of interest within the scanned granules. Due to the varying densities found within a sample, highly attenuating regions will absorb more X-ray photons, leading to lighter grey colours in the CT reconstructions (Kirz et al., 1986). A multistep segmentation method can then be used to separate the granule from the surrounding air and supports, similar to the methods used by Danalou et al. (Zeinali Danalou et al., 2023). An example of the segmentation process can be seen in Fig. 4.

Firstly, the upper half of the grayscale histogram values can be separated by the upper Otsu method, with the granule further isolated by removing the supports by subtracting a mask from the region of

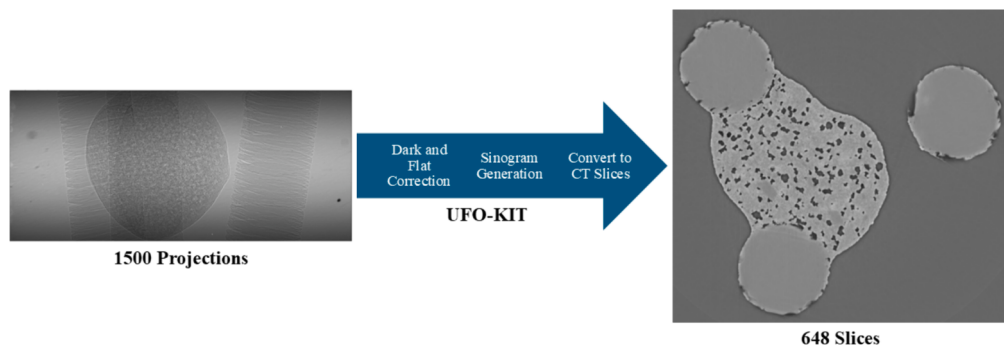


Fig. 3. Example of the CT reconstruction process using the collected X-ray projections for 80LMH20APAP sample.

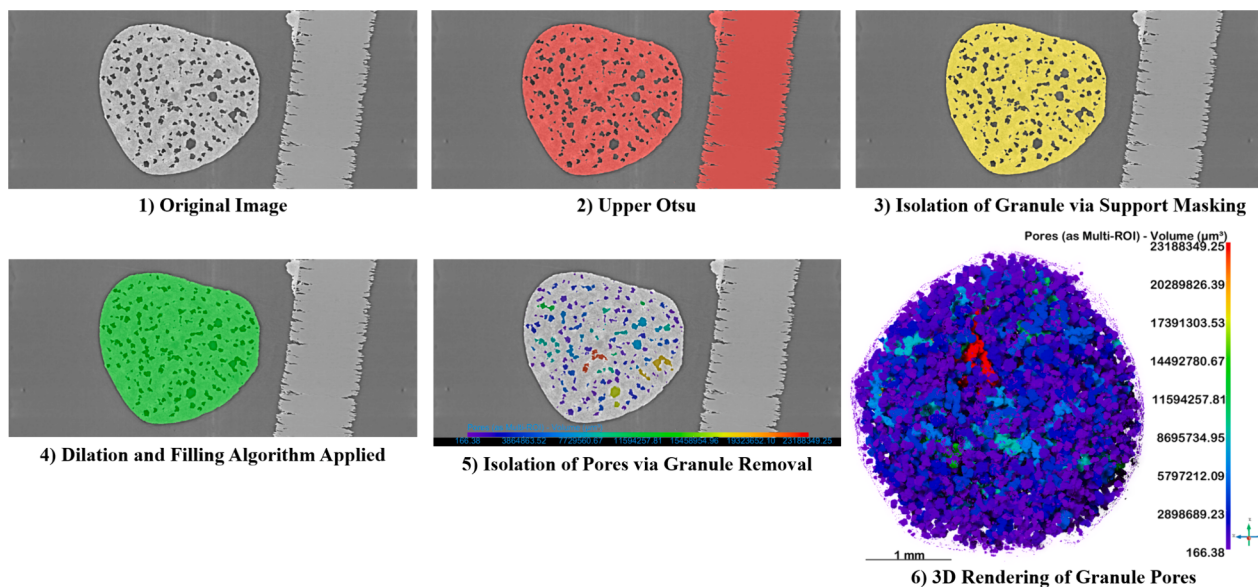


Fig. 4. Segmentation process and 3D rendering for the pore volume in an 80LMH20APAP sample.

interest (ROI). A dilation algorithm was then applied to a copy of the granule ROI to include all pores inside the granule, and the pores were then isolated by subtracting the granule ROI from the dilated copy. Lastly, 3D volume rendering was used, and histogram data of the regions of interest were extracted. Quantified data was imported into SPSS statistics 28 to determine significance using ANOVA testing, with OriginPro 2021b used for graph generation and nonlinear curve fitting with results from SPSS using the least squares method.

4. Results and discussion

During the drying process, granules of pure components and mixtures were evaluated for internal structural changes within the pore volume, with further information gained through analysis of the gray-scale histograms obtained for the entire region bounded by the granule's surface as seen in step 4 of Fig. 4. To verify the results for air and water contents, the fractional results within the volume of voids were brought into fraction forms for all samples and time points, with the underlying volume balance within the voids adding to unity. Pure components of APAP, MCC, LMH, and CBZ were investigated, with binary mixtures composed of 90 % to 50 % excipient by weight (MCC or LMH) with the remainder being an API (APAP or CBZ). Two common excipients were used to compare their nature of drying in addition to API loading, with the selected APIs used to compare the hydrophilic nature of APAP to the moderately hydrophobic nature of CBZ (Barakat et al., 2008; Maswal et al., 2013). Initial moisture contents were measured at 30 % for all

samples, apart from pure LMH which was limited to 25 % moisture content due to dissolution effects occurring at higher moisture contents. Ten interval scans were performed, with one scan taken every minute from 0 to 5 min, with the remaining scans taken at 5-minute intervals. The aim in the selection of these intervals was to capture the initial stages of drying as rapidly as possible with the given 1500 projections, with changes observed after the first 5 min being relatively constant.

4.1. Pore volume

To better understand the internal changes and map pore size distribution, 3D volume rendering was applied to the segmented data. A time series example of this can be seen in Fig. 5, with the respective time series data shown in Fig. 6.

As can be seen in Fig. 5, the initial granules have a uniform pore distribution, with many small pores isolated within all parts of the granule. As drying is introduced, the individual pores begin to shrink and connect into a much larger pore network, with connectivity occurring from the outermost regions of the granule, with connections forming from the edge to the center. This is consistent with the drying mechanism of porous materials, with pockets of air observing an affine shrinkage as adjacent pores lose moisture and begin to merge with one another, resulting in the formation of a larger, interconnected void space (Lesov et al., 2014; Hamamoto et al., 2022). The air evolution within the pore volume of the granules is quite uniform from the quantified results, as seen in Fig. 6, with a gradual increase observed for all samples, not

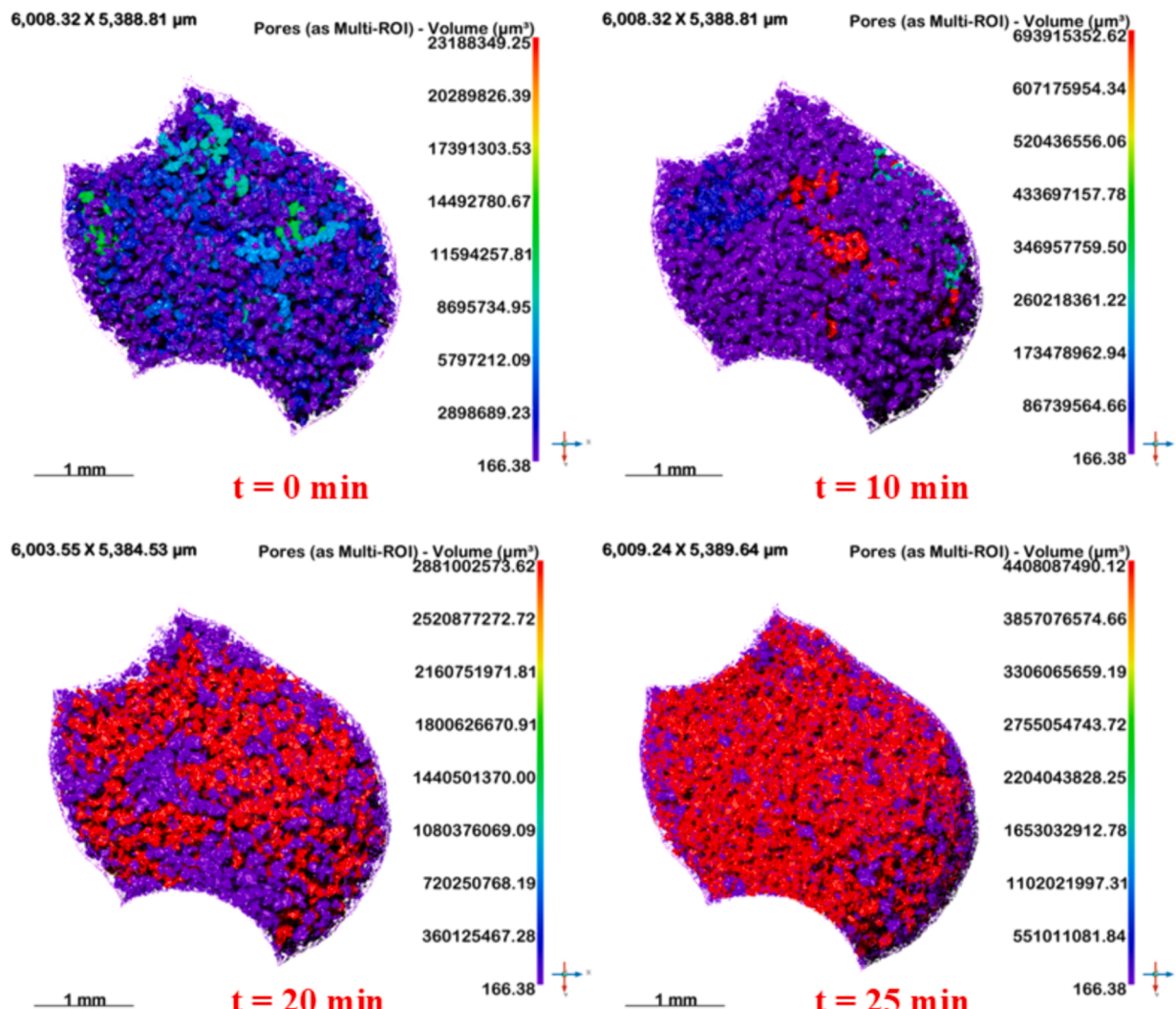


Fig. 5. 3D Rendering of the pore volume changes over a 25 min drying time for an 80LMH20APAP sample at 0.10 m/s and 25 °C.

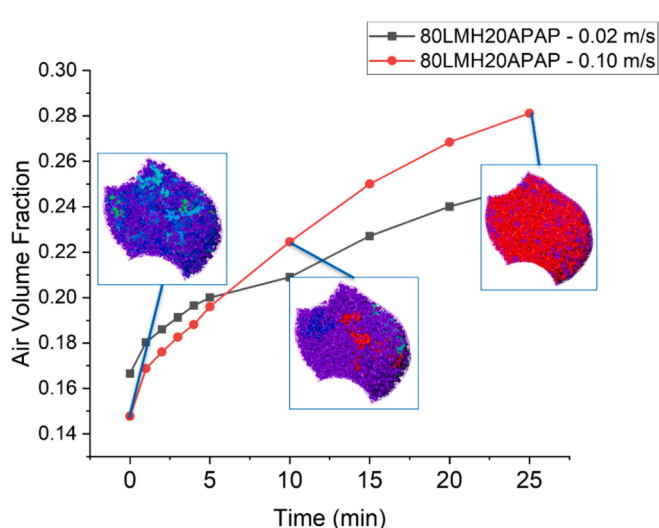


Fig. 6. Quantified changes to the pore volume for 80LMH20APAP at 0.02 m/s and 0.10 m/s at 25 °C.

observing any sharp changes with an increase in the drying time.

Within the first 5 to 10 min, this pore network development can be observed, generating large, interconnected pockets of air within the granules. This connective behaviour continues until most of the pores create a singular pore network of up to 38 % of the granule's volume, with further drying allowing for additional smaller pores surrounding the single larger network to become connected.

For materials such as APAP that are noted to be hydrophilic, the generation of the fully developed pore network is observed to be very slow under mild drying conditions, with little pore growth and connection occurring beyond a relatively sharper initial increase. With an increase in the gas velocity and temperature, this change in the pore network becomes much more apparent, with larger amounts of air found within the pore volume at the end of drying. The changes to the air volume fraction for APAP can be seen in Fig. 7. As hydrophilic materials exhibit an affinity for water, the distribution of water within the material is likely to be more uniform, resulting in an existing pore network with minimal closed pores as moisture evaporation is permitted. Comparatively, CBZ, which is shown to be moderately hydrophobic, maintains moderate pore network growth at both mild and elevated drying conditions, as illustrated in Fig. 8. As hydrophobic materials resist wetting, larger initial pores may be exhibited and result in larger void spaces within the material as the drying process proceeds, with a greater contribution of air to the pore volume as moisture is removed.

Comparing the excipients' drying behaviour, both MCC and LMH see

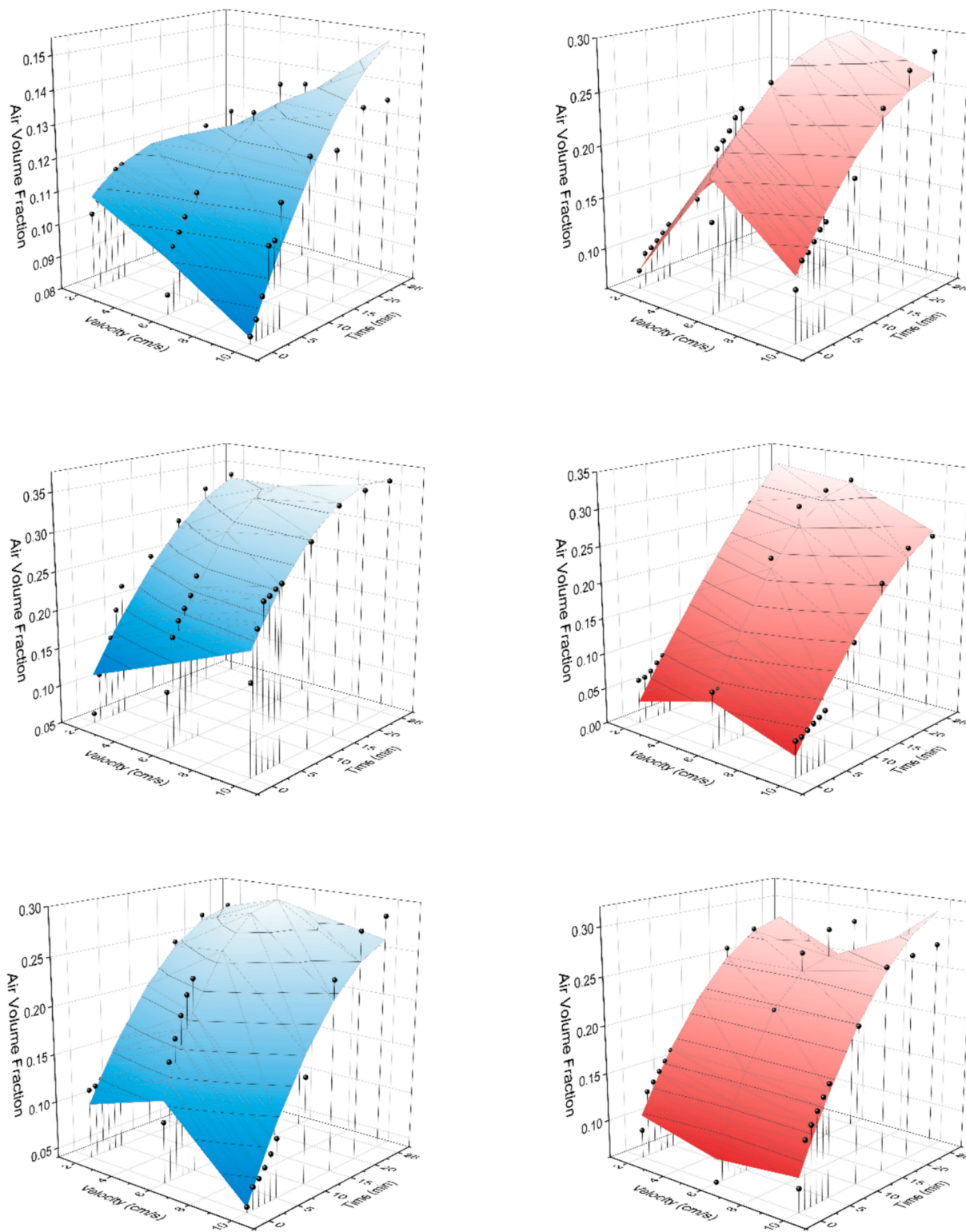


Fig. 7. APAP, MCC, and LMH data points and fitted surfaces for the air volume changes observed during the drying process for increasing velocity and increasing temperature (25 °C in blue, 40 °C in red). (Top left: APAP – 25 °C, Top right: APAP – 40 °C, Middle left: MCC – 25 °C, Middle right: MCC – 40 °C, Bottom left, LMH – 25 °C, Bottom right: LMH – 40 °C).

a similar drying pattern, with steady changes to the pore network in Fig. 7 similar to that shown in Fig. 5. However, granules containing MCC have been observed to shrink during the drying process, decreasing by up to 25.2 % in volume. Compared to the other pharmaceutical materials tested, this shrinking behaviour is not observed for APAP, LMH, or CBZ, with this change only observed in pure MCC, binary mixtures of

MCC/APAP with higher MCC loadings, and mixtures with CBZ. The shrinkage of the MCC granules has been observed to be a complex process influenced by the trapping of water in fine capillaries and internal pores, with methods such as hot air over-drying being considered slower in terms of a water removal mechanism than methods such as freeze-drying, allowing for the solid material to shrink by capillary

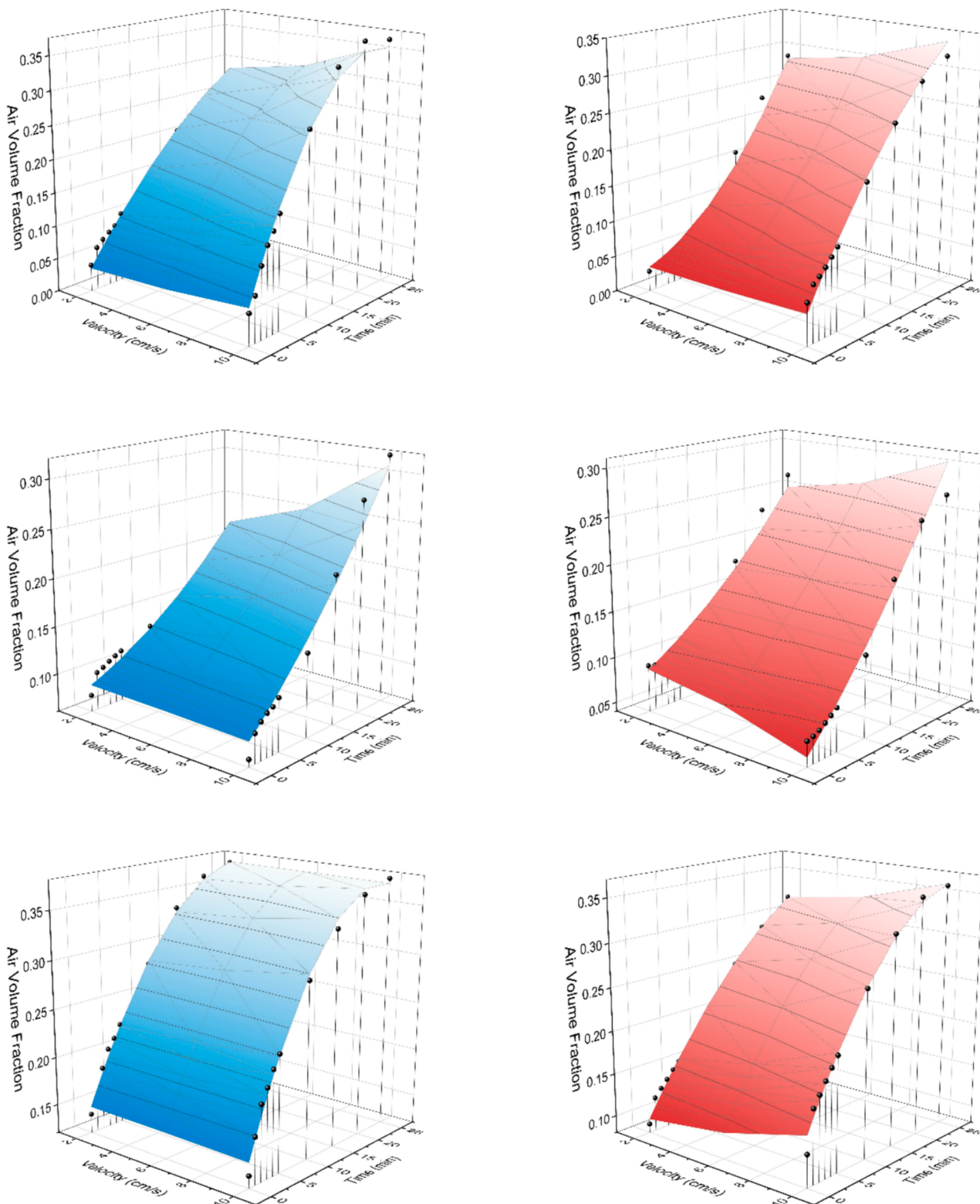


Fig. 8. CBZ, 50MCC50CBZ, and 50LMH50CBZ data points and fitted surfaces for the air volume changes observed during the drying process for increasing velocity and increasing temperature (25 °C in blue, 40 °C in red). (Top left: CBZ – 25 °C, Top right: CBZ – 40 °C, Middle left: 50MCC50CBZ – 25 °C, Middle right: 50MCC50CBZ – 40 °C, Bottom left, 50LMH50CBZ – 25 °C, Bottom right: 50LMH50CBZ – 40 °C).

forces resulting from the high surface tension of water (Bashaiwoldu et al., 2004).

The effect of API loading on the development of the air volume fraction within the pore network can be seen in Figs. 8–10. With an increase of APAP loading on both excipients, the coalescence of the pores

shifts toward the drying behavior of pure APAP, with this effect predominant in binary samples where LMH is the excipient. As LMH tends to be freely soluble in the presence of moisture, the dominant hydrophilic effects of APAP are expected to be more influential in the development of the pore structure, whereas MCC is insoluble in water,

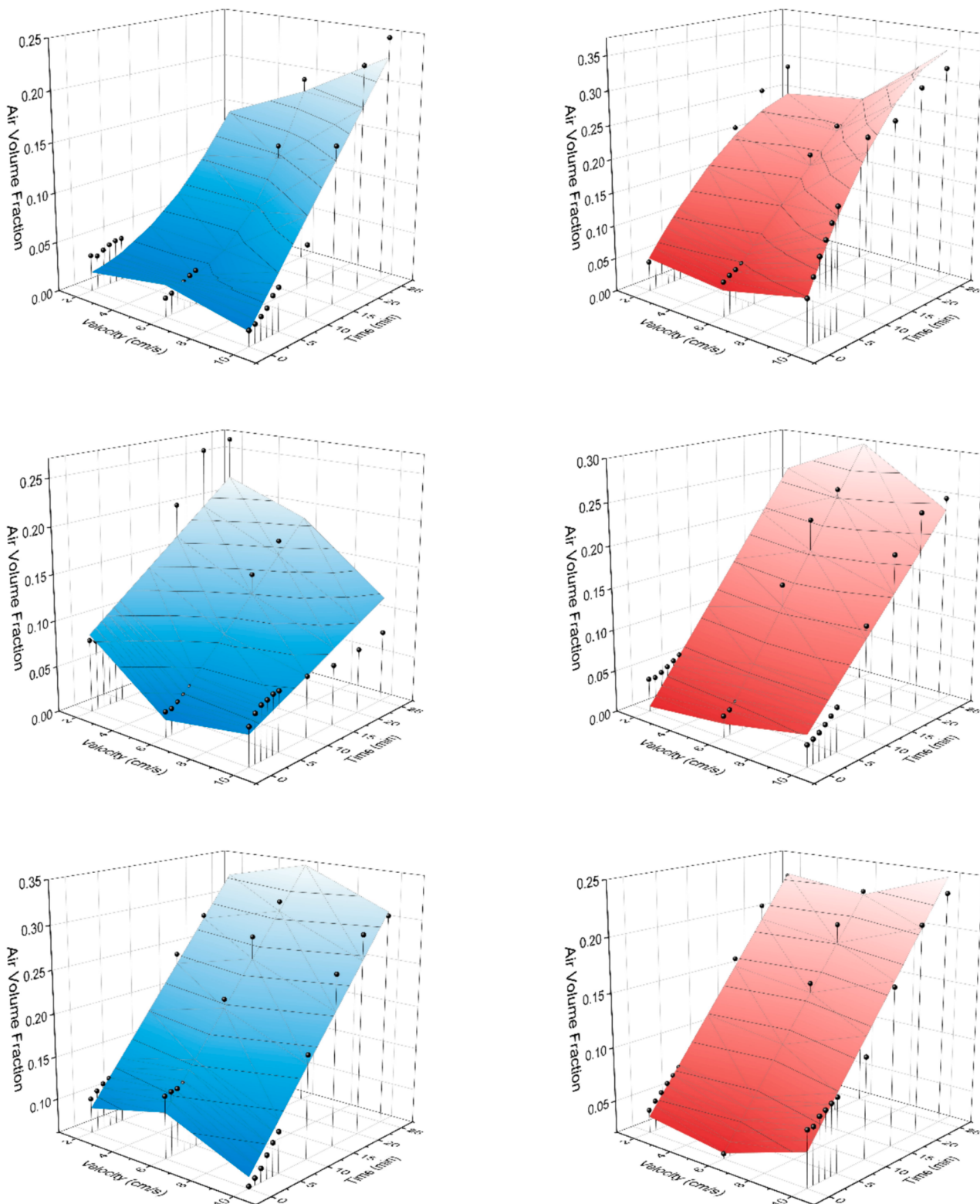


Fig. 9. 90MCC10APAP, 80MCC20APAP, and 50MCC50APAP data points and fitted surfaces for the air volume changes observed during the drying process for increasing velocity and increasing temperature (25 °C in blue, 40 °C in red). (Top left: 90MCC10APAP – 25 °C, Top right: 90MCC10APAP – 40 °C, Middle left: 80MCC20APAP – 25 °C, Middle right: 80MCC20APAP – 40 °C, Bottom left, 50MCC50APAP – 25 °C, Bottom right: 50MCC50APAP – 40 °C).

allowing for the material properties to contribute to the solid fraction within the granule. Conversely, the binary mixtures with CBZ and the excipients were not observed to be significantly influenced by API loading as CBZ is moderately hydrophobic in nature, with the evolution of the air volume fraction comparable to the pure components.

A summary of the changes observed within the pore volume can be seen from the ANOVA results depicted in Table 3. All samples tested were included, with parameters of temperature, velocity, and time tested for each sample set. It should be noted that the results were also tested for sample composition across all samples, with the results finding

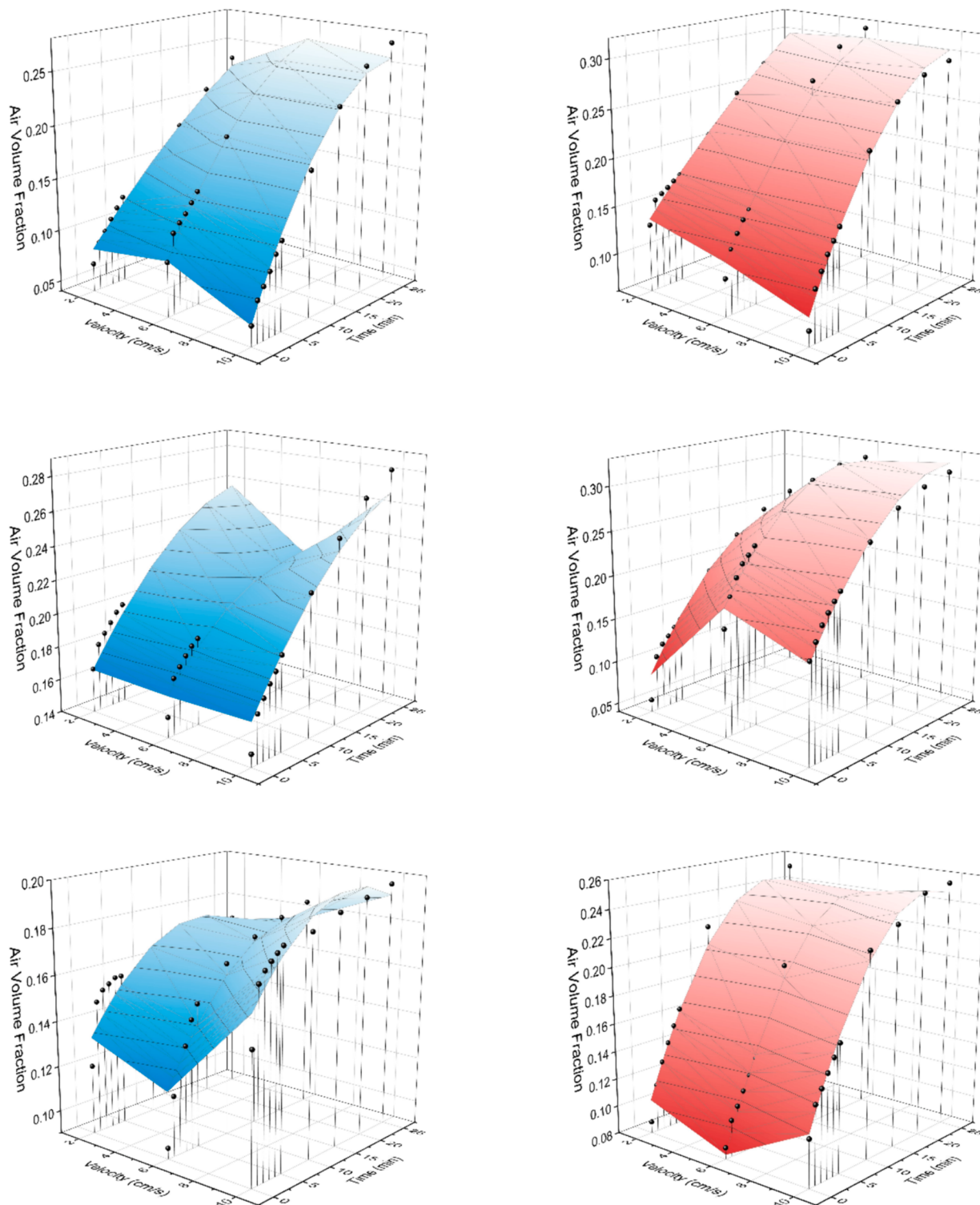


Fig. 10. 90LMH10APAP, 80LMH20APAP, and 50LMH50APAP data points and fitted surfaces for the air volume changes observed during the drying process for increasing velocity and increasing temperature (25 °C in blue, 40 °C in red). (Top left: 90LMH10APAP – 25 °C, Top right: 90LMH10APAP – 40 °C, Middle left: 80LMH20APAP – 25 °C, Middle right: 80LMH20APAP – 40 °C, Bottom left: 50LMH50APAP – 25 °C, Bottom right: 50LMH50APAP – 40 °C).

significant influence from the sample composition on the pore volume changes with a p-value <0.001 (significance <0.05).

Of the changes observed within the pore volume, it is most notable that a significant change in the air fraction occurs for all samples throughout the drying time as expected. For all samples, apart from APAP at 25 °C, an increase in the air fraction within the pore volume was observed. These changes were quantified, with the initial air volume

fraction being as low as 0.02 and increasing to as much as 0.38 throughout the drying process. Pure APAP samples and higher loadings of APAP observe changes in the air volume fraction between 0.02 and 0.31, with increasing gas velocity and temperature increasing the change in the air volume within the samples. All samples containing CBZ are observed to have changes in the air volume fraction between 0.03 and 0.38, with very little variance between samples dried at different

Table 3

ANOVA results for the significance of investigated variables on the pore volume.

| Material | Drying time significance | Drying air velocity significance | Drying air temperature significance |
|-------------|--------------------------|----------------------------------|-------------------------------------|
| APAP | 0.206 | 0.003 | <0.001 |
| MCC | <0.001 | 0.419 | <0.001 |
| LMH | <0.001 | 0.468 | 0.755 |
| 90MCC10APAP | <0.001 | 0.112 | <0.001 |
| 80MCC20APAP | <0.001 | 0.492 | 0.498 |
| 50MCC50APAP | <0.001 | 0.957 | 0.001 |
| 90LMH10APAP | <0.001 | 0.788 | 0.016 |
| 80LMH20APAP | <0.001 | 0.031 | 0.483 |
| 50LMH50APAP | <0.001 | 0.095 | 0.281 |
| CBZ | <0.001 | 0.049 | 0.249 |
| 50MCC50CBZ | <0.001 | 0.618 | 0.738 |
| 50LMH50CBZ | <0.001 | 0.262 | 0.121 |

drying gas velocities and temperatures. Excipient samples of MCC have an air volume fraction increase from 0.02 up to 0.36, and LMH samples change from 0.05 up to 0.31. Effects of drying gas velocity and temperature were found to be of mixed significance depending on the composition and API loading for both excipients.

With increasing the gas velocity, significant changes were found for both pure API's in addition to 80LMH20APAP. For APAP, the hydrophilic nature of the material requires elevated drying conditions to better liberate any bound water, opening the pore network to allow air to occupy the volume. With CBZ already being moderately hydrophobic, the water within the samples does not require much energy input for evaporation to occur, with an increase in velocity removing the moisture at an increased rate as expected, thus increasing the air volume changes within the pore network. While the pore network of pure LMH was not found to be significantly impacted by increasing the air velocity, increasing velocity was found to be significant at moderate APAP loadings within the binary mixtures. This is likely due to a region between pure LMH and pure APAP loadings, where the drying does not become too dominated by either material's inherent properties, and the changes in the pore volume are permitted with increasing velocity affecting the removal of moisture and increase in air volume within the pore volume. Additionally, the soluble nature of LMH allows for APAP to present itself more dominantly within the solid fraction of the granules. The remaining granules' pore volume changes were not found to be significantly influenced by an increase in the drying air velocity.

The effect of temperature on the pore volume changes was found to have mixed significance depending on the material. Both pure APAP and MCC were found to be significantly influenced by an increase in temperature, with 90MCC10APAP, 50MCC50APAP, and 90LMH10APAP also observing this change. Similar to the changes to APAP observed with increasing velocity, an increase in drying air temperature promotes evaporation, better allowing the material to be liberated of moisture due to the increased energy. For MCC, the sloped regions following the initial stages of drying can be seen to be much steeper with an increase in drying air temperature, again resulting in the promotion of evaporative forces and the displacement of moisture within the granules with air. For the binary mixtures, the compositions of MCC/APAP are within regions close to either pure APAP or pure MCC, with similar phenomena expected similarly to that behaviour observed in the pure components. For the 90LMH10APAP samples, the effects of the pure components are not dominated by one or the other at this composition, allowing for temperature changes to significantly affect the changes to the pore volume. The remaining samples' pore volume changes were not found to be significantly influenced by an increase in the drying air temperature.

In comparing the differences between APIs and the drying behaviour observed, the effect of hydrophilicity and hydrophobicity can be discussed. Comparing results for 25 °C experiments, APAP does not produce much change within the pore volume due to the material's hydrophilic nature, maintaining a low pore volume fraction in the

region of 0.11, while CBZ can change from 0.03 to 0.37. Introducing temperature changes, CBZ still follows a similar trend, while APAP is now capable of changing up to a pore volume fraction of 0.28. This again demonstrates the expected moisture liberation of hydrophilic materials, with the increase in energy better allowing for moisture removal through evaporation, with this removal being replaced with the surrounding air in a more efficient removal as hydrophilic materials maintain a more prevalent and interconnected pore structure (Thomik et al., 2022). With the addition of excipients, CBZ maintains its drying behaviour, having minimal effects on the drying behaviour of the excipients, while APAP exhibits more of a dominance on the drying pattern of the excipients, trending closer to the drying behaviour of pure APAP at higher API loadings. Within the individual pore volumes, as the water evaporates during the hot air drying process, the pore structure and stability for each API is are susceptible to collapse and deformation as the drying rate increases resulting from an increase in the drying gas velocity and temperature. APAP was observed to dry out much more rapidly with increasing the drying conditions, as indicated by the overall changes to the total pore volume as seen in Fig. 7. Furthermore, the time series CT reconstructions revealed moderate pore collapsing within the increased conditions, with individual micro-pores increasing the connectivity between macro-pores as they expand into one another before deforming. In contrast, the drying of CBZ was not observed to encounter structural issues, as the lack of strong water interaction allows for the moisture to be removed freely as seen between all conditions in Fig. 8, with pore collapse not observed in the time series CT reconstructions.

To examine the reproducibility of the experiments, three replicates each of LMH at 0.10 m/s at 25 °C and 40 °C were processed respectively. The results for the air volume fraction changes can be seen in Fig. 11.

Similar to those results seen in Fig. 7, the air volume fraction within the pores of the granules increases for both temperatures as drying continues, with the effect of temperature accelerating this change. The curves are consistent with those results seen in Fig. 7, with acceptable deviations observed between the error bars and data points seen in Fig. 11 and the data points seen in Fig. 7.

4.2. Moisture ratio

Alongside the 3D volume rendering, grayscale histograms were obtained for each time point during granule drying, covering the range of the entire granule and its pores. Contributions to the grayscale histograms include various attenuations from the air fraction within the pores, the moisture within the granule, and the solids of pharmaceutical materials. An example of these histograms can be seen in Fig. 12.

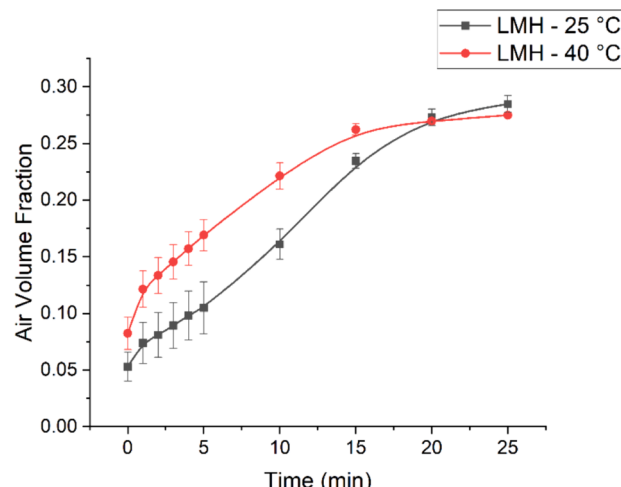


Fig. 11. Quantified changes to the pore volume for LMH replicates at 25 °C and 40 °C at 0.10 m/s to determine repeatability.

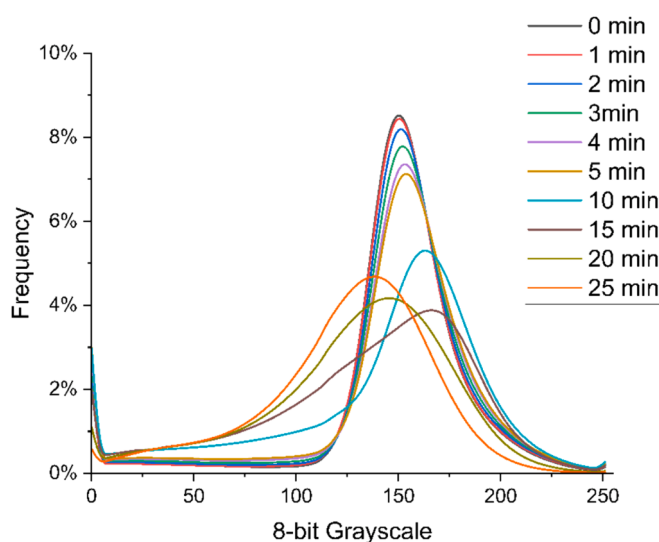


Fig. 12. Grayscale histogram curves taken from the reconstructed CT data for the drying of MCC at 0.06 m/s and 40 °C.

Initially, the wet granules see larger peak values trending toward the right-hand side of the plot, attributed to the higher moisture and pharmaceuticals within the sample, with a smaller peak towards the left-hand side of the plot, attributed to the lower air volume within the sample. As the granule undergoes drying, the peak values for the attenuation of the pharmaceutical materials and the moisture decrease, while an increase is observed in the peak values for the air content, seeing an overall shift of the curve downward and toward the lower left grayscale values. To illustrate the effects of moisture and air on the grayscale distribution, reference samples of pure components were processed and their values are shown in Fig. 13.

To determine the moisture content at each time step within the granule, the segmented air volume fraction at each time step can be used to determine its contribution to the grayscale attenuation, with the contribution of any moisture within the air being negligible in comparison to the bound moisture within the solid fraction. The segmented X-ray intensity was determined from the grayscale values of each sample and control reference, a common method used in X-ray imaging for quantitative analysis (Kelkar et al., 2015). Values representing an attenuation are then used with the Beer-Lambert Law (Mayerhöfer et al.,

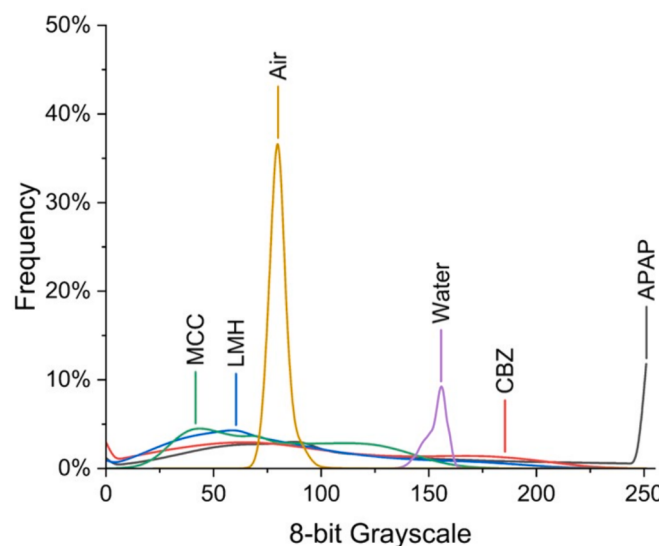


Fig. 13. Grayscale histogram curves for pure components.

2020) in conjunction with the given sample thickness to determine the overall linear attenuation coefficients for a sample.

$$\frac{N}{N_0} = \exp(-\mu l) \quad (7)$$

where N/N_0 is the attenuation; μ is the linear attenuation coefficient; l is the sample thickness.

In addition to the obtained values, pure components of the pharmaceutical materials, water, and air were also determined to help calibrate the moisture content prediction. Using the known air volume fraction and the calculated overall linear attenuation coefficient for a sample at each given time, the moisture content at each time step can be calculated by an equation similar to Eqs. (3) and (4):

$$\mu = (\mu_s * (1 - X) + \mu_w * X)(1 - \varepsilon) + \mu_a * \varepsilon \quad (8)$$

where μ is the overall linear attenuation coefficient; μ_s is the linear attenuation coefficient of the pharmaceutical solids; μ_w is the linear attenuation coefficient of water; μ_a is the linear attenuation coefficient of air; X is the moisture content; ε is the air volume fraction. The initial moisture content (X_0) and each time point for moisture content (X) can be used to determine the moisture ratio (MR) plots.

A summary of the changes observed in the moisture ratio can be seen from the ANOVA results depicted in Table 4. All samples tested were included, with parameters of temperature, velocity, and time tested for each sample set. It should be noted that the results were also tested for sample composition across all samples, with the results finding significant influence from the sample composition on the moisture ratio changes with a p-value <0.001 (significance <0.05).

Within the observed changes to the moisture ratio, the drying time significantly influences changes in the moisture ratio as expected for all samples. As seen in Figs. 14-17, both the experimental data and the fitted curves follow a decreasing trend, which is expected for drying processes, with moisture content gradually decreased as factors of drying time, drying gas flow rate, and temperature increase (Silva et al., 2017; Susrala et al., 2013). This is easily seen in examples such as 80LMH20APAP in Fig. 16, where the increase in velocity allows for a larger decrease in the moisture ratio, with increasing temperature observed to further decrease the moisture ratio over the same drying time. The drying time for all samples is comparable to results seen in methods such as acoustic levitation or a drying channel, with curve shapes similar to larger scale drying operations such as the use of fluidized bed drying for pharmaceutical granules (Groenewold et al., 2002; Li et al., 2022). This similarity is predominant in granules with 10 % to 20 % APAP loading for both MCC and LMH at higher temperatures, where the effects of increasing the drying gas velocity and temperature are more noticeable, although with a much shorter drying time resulting from the use of stationary single granules as compared to an entire bed of

Table 4
ANOVA results for the significance of investigated variables on the moisture ratio.

| Material | Drying time significance | Drying air velocity significance | Drying air temperature significance |
|-------------|--------------------------|----------------------------------|-------------------------------------|
| APAP | <0.001 | 0.449 | 0.025 |
| MCC | <0.001 | 0.944 | 0.004 |
| LMH | <0.001 | 0.398 | 0.514 |
| 90MCC10APAP | <0.001 | 0.031 | 0.262 |
| 80MCC20APAP | <0.001 | 0.081 | 0.258 |
| 50MCC50APAP | <0.001 | 0.851 | 0.05 |
| 90LMH10APAP | <0.001 | 0.283 | 0.761 |
| 80LMH20APAP | 0.01 | 0.058 | <0.001 |
| 50LMH50APAP | <0.001 | 0.419 | <0.001 |
| CBZ | <0.001 | 0.498 | 0.887 |
| 50MCC50CBZ | <0.001 | 0.019 | 0.723 |
| 50LMH50CBZ | <0.001 | 0.428 | 0.691 |

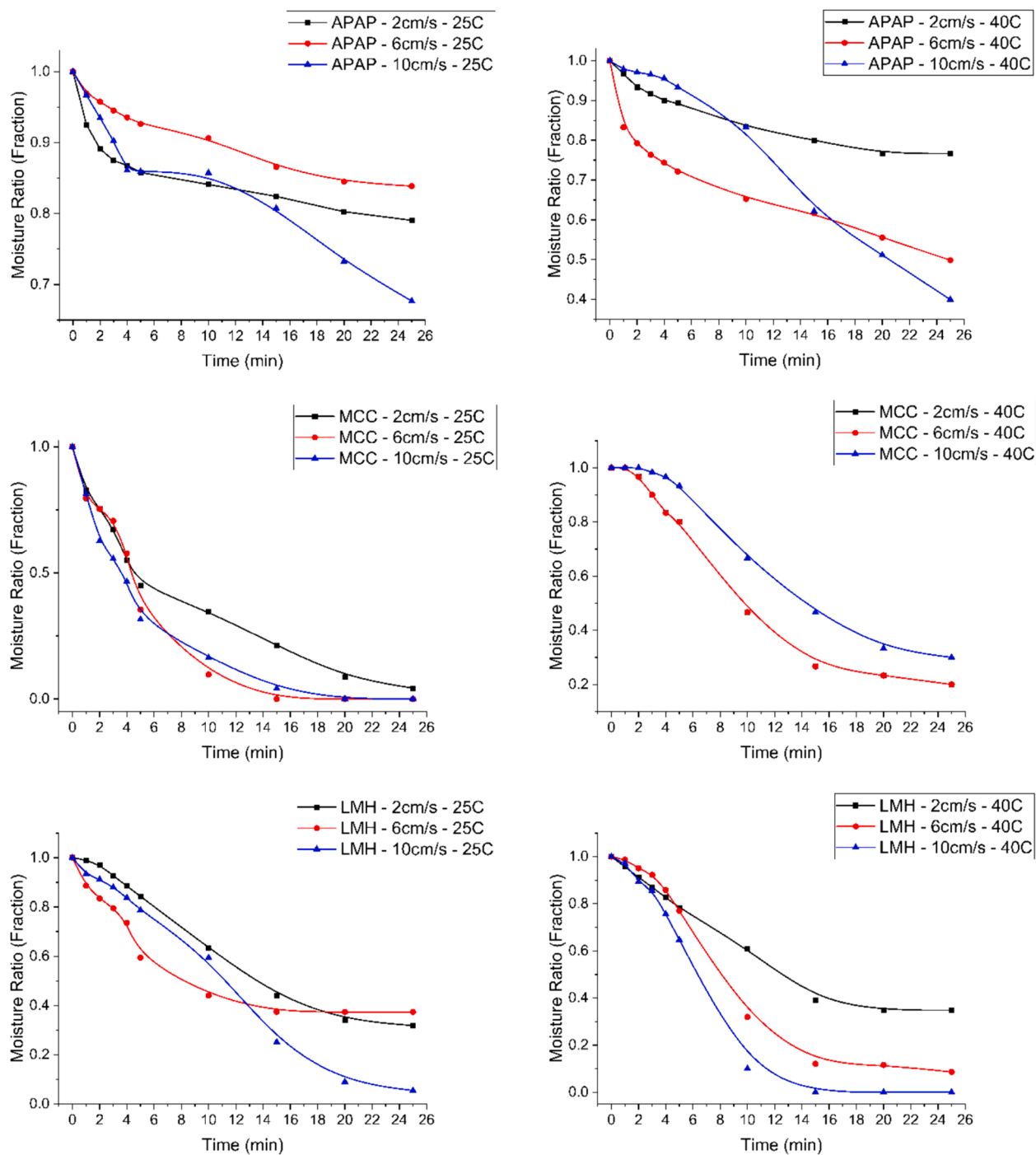


Fig. 14. Comparison of the experimental data and fitted curves of moisture ratio for single granule drying of pure APAP, MCC, and LMH granules.

fluidized material (Li et al., 2022).

The effects of the drying air velocity are observed to have mixed significance on the changes to the moisture ratio of the investigated pharmaceuticals, with 90MCC10APAP and 50MCC50CBZ being significantly influenced. These changes show a significant decrease in the time required to achieve a lower moisture ratio as the drying air velocity is increased, while all other samples exhibited similar drying patterns for different velocities. The result of the drying air velocity not being overly significant in influencing changes in the moisture content and the drying kinetics may be attributed to capillary action and a strong retention of water molecules within hydrophilic, colloidal, organic materials (Said et al., 2015; Li et al., 2021).

Similar to the results for the effects of velocity, the effect of

temperature was found to be of mixed significance on the changes to the moisture ratio. Pure APAP and MCC samples were found to be significantly influenced by an increase in the drying air temperature, with higher loadings of APAP in binary mixtures with excipients also being significantly impacted. While temperature changes were not found to significantly influence the drying of pure LMH, loadings of 20 % to 50 % APAP were found to be significant, exhibiting a shift from the drying of pure LMH as the drying becomes more dominated by the drying behaviour of APAP. Interestingly, the 50LMH50APAP group subject to the drying temperature of 40 °C as seen in Fig. 16 is observed to have a larger decrease in the moisture ratio at lower velocities. From the 3D reconstructions of the data, the 50LMH50APAP granules are observed to form the surface crust much faster from the combined effects of

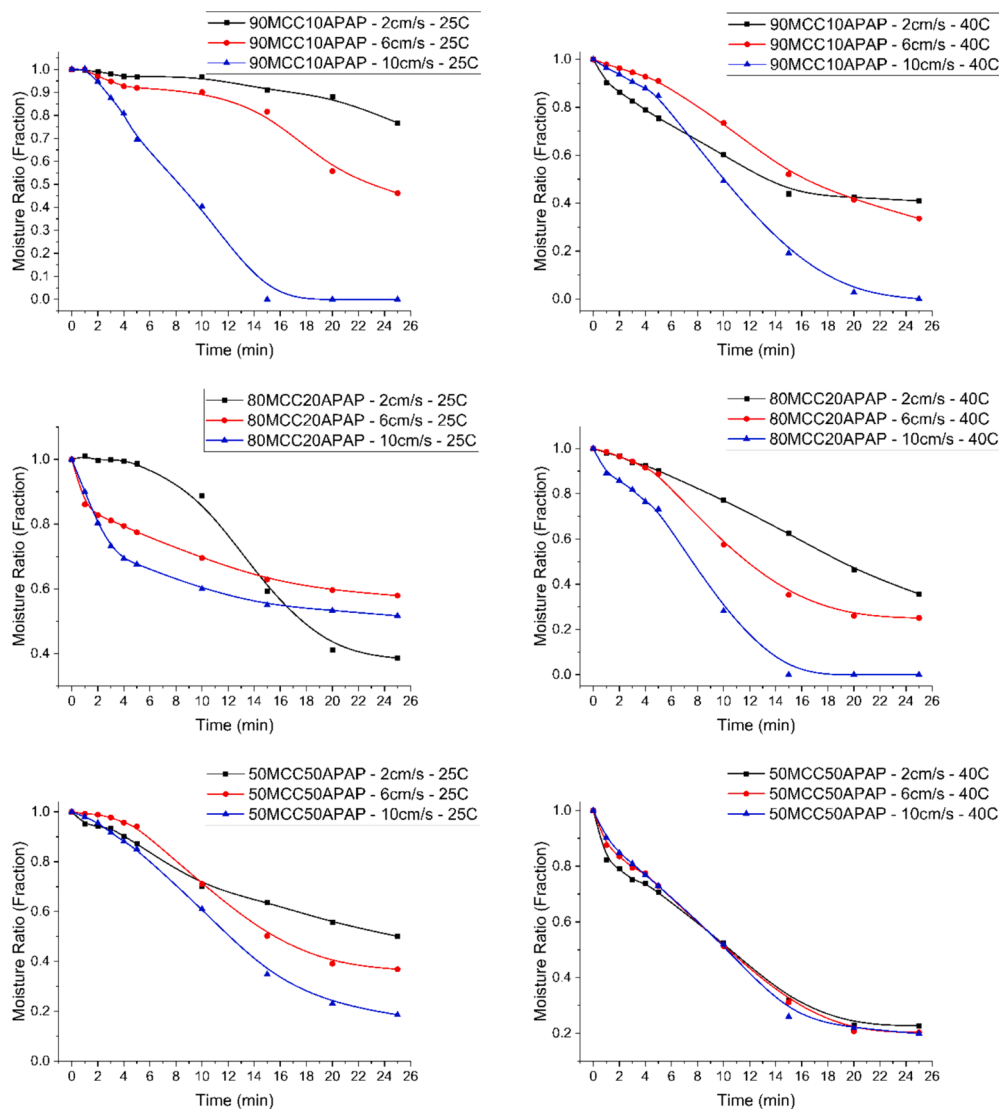


Fig. 15. Comparison of the experimental data and fitted curves of moisture ratio for single granule drying of MCC/APAP binary granules.

increased temperature and velocity, inhibiting the removal of moisture and trapping water within the center of the granules. By decreasing the velocity, the increased temperature can still allow for the promotion of moisture transfer from the material to the surrounding air without the crust forming as rapidly, where diffusion and evaporation would be limited. APAP loadings of 50 % were found to be significant on the drying of MCC, again showing a trend toward APAP dominating the drying behaviour at higher API loadings as a result of the hydrophilic nature of APAP. Increased loading of the moderately hydrophobic CBZ was not shown to have any difference in the drying behaviour of its pure component and in binary mixtures with pharmaceutical excipients for an increase in temperature. For the samples where the drying gas velocity may not be significant while still being significantly influenced by temperature, it is indicative of temperature overriding the effects of capillary action and water retention; the vapour pressure of the surrounding air further promoting the transfer of moisture from the material to the surrounding air by diffusion as the increase in energy increases the evaporation rate with a higher temperature gradient observable between the drying gas and the granules surface (Li et al., 2022; Salager et al., 2010; Akpinar and Toraman, 2016).

Comparing the excipients of MCC and LMH, the materials possess drastically different mechanisms when in contact with water. While lactose is observed to dissolve directly into water and form pastes, MCC

exhibits a swelling within the fine capillaries of the material as moisture is introduced (Kytä et al., 2020). Conversely, during the drying process by means of hot air, LMH is permitted to reform as the solvent evaporates and the concentration of the dissolved materials increases. However, the trapped moisture within the swelled MCC granules fine capillaries and internal pores pulls on the bounded regions as evaporation occurs due to capillary action resulting from the high surface tension of water (Bashaiwoldu et al., 2004).

The differences of the two APIs tested can also be compared, with several notable differences observed as a result of the difference in hydrophilicity and hydrophobicity. While the effect of temperature does not significantly influence the drying behaviour of CBZ, the increase in energy permits the bound water of APAP granules to be liberated more easily, significantly decreasing the moisture ratio. This is likely due to the hydrophilic nature of APAP, as the bound water will require a higher energy input for evaporative effects to occur more efficiently. For the API loadings on both excipients, CBZ was not shown to impact the drying behaviour of either MCC or LMH, with results comparable to the drying of their respective pure components. However, by increasing the loading of APAP on either excipient, the drying behaviour became more dominated by the hydrophilic effects of APAP, with the drying nature trending more toward the behaviour of pure APAP.

Resulting from the changes to the pore volume as the individual

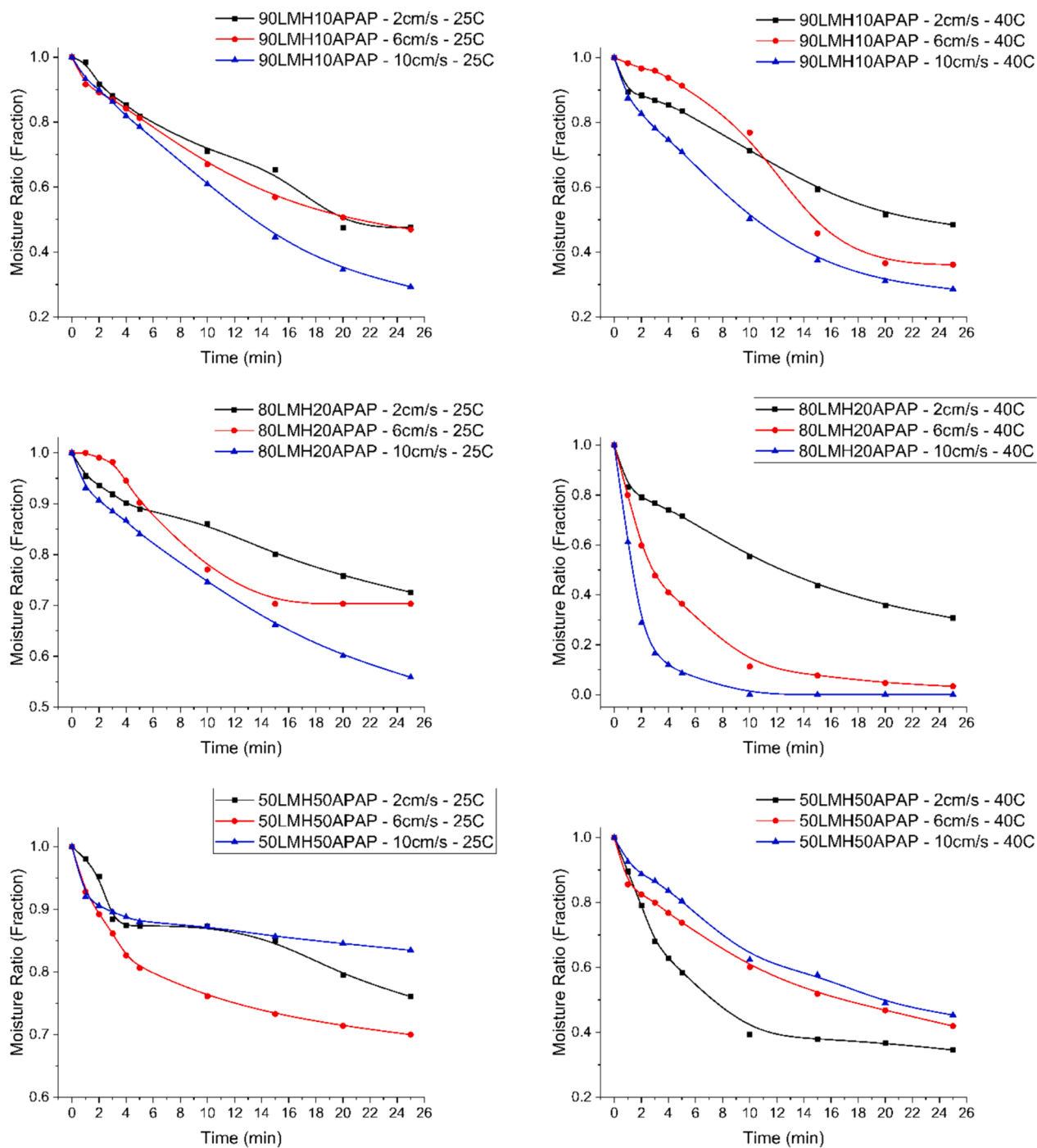


Fig. 16. Comparison of the experimental data and fitted curves of moisture ratio for single granule drying of LMH/APAP binary granules.

granules structure is influenced by the changes in moisture content, the single granules hardness is subject to changes influenced by pore properties (Zeinali Danalou et al., 2023; Grote and Kleinebudde, 2018). Before the drying process, the granules higher initial moisture content creates a soft and flexible internal structure. As drying is introduced and moisture is permitted to evaporate, the pore volume changes, and the individual granules become more rigid. As observed by Danalou et al. (Zeinali Danalou et al., 2023), an individual granule with lower porosity and finer pores exhibits a higher hardness, with materials such as LMH possessing a higher hardness from a smaller mean pore volume. For all of the samples used in this study, the coupled pore volume and moisture content changes can be used to evaluate the hardness of the produced

granules. For all materials, the increase in the temperature and velocity of the drying air enhances the efficiency of moisture removal and will generally increase the hardness, although excessive conditions may lead to degradation and impacts on the granule quality resulting from uneven drying (Gilpin and Zhou, 2004), with the decreased moisture content and pore volume of samples consisting of LMH and 80LMH20APAP consistent with higher hardness findings from Danalou et al. (Zeinali Danalou et al., 2023).

To examine the reproducibility of the experiments, three replicates each of LMH at 0.10 m/s at 25 °C and 40 °C were processed respectively. The results for the moisture ratio changes can be seen in Fig. 18.

Similar to those results seen in Fig. 14, the moisture ratio decreases

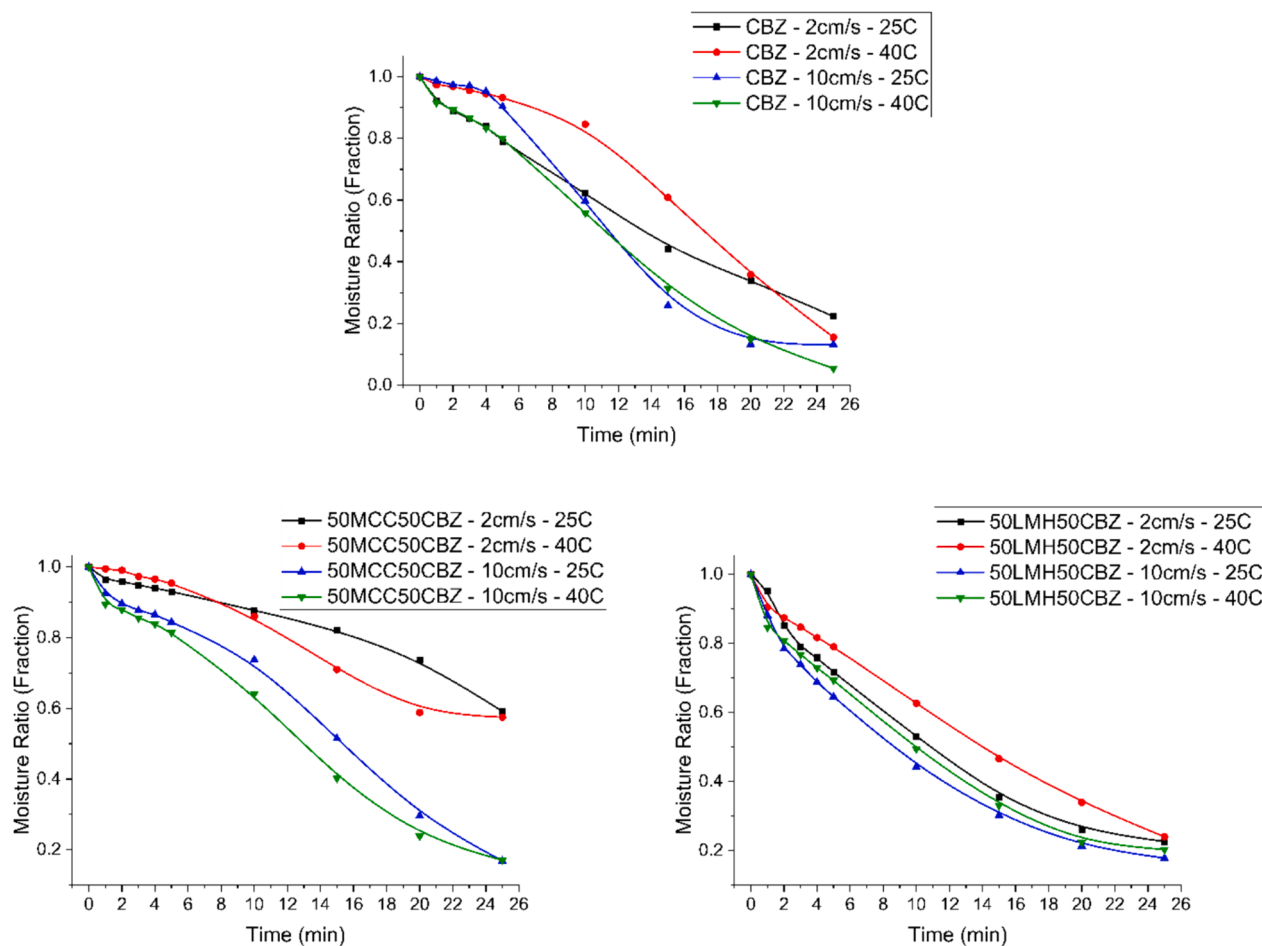


Fig. 17. Comparison of the experimental data and fitted curves of moisture ratio for single granule drying of pure CBZ and excipient/CBZ binary granules.

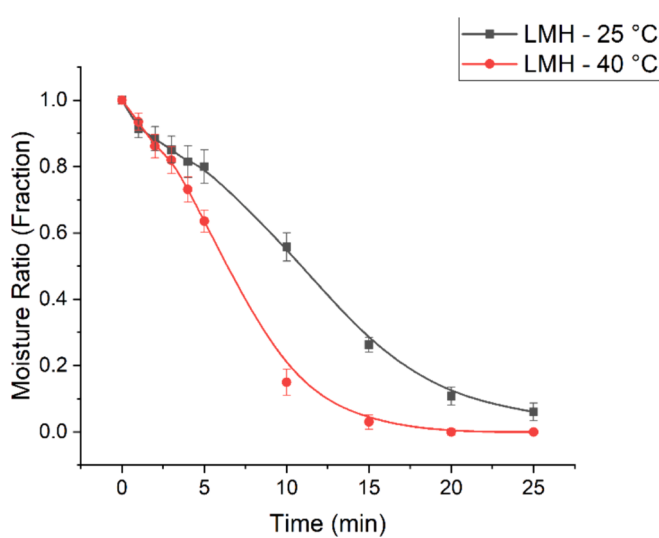


Fig. 18. Quantified changes to the moisture ratio for LMH replicates at 25 °C and 40 °C at 0.10 m/s to determine repeatability.

for both temperatures as drying continues, with the effect of temperature accelerating this change. The curves are consistent with those results seen in Fig. 14, with acceptable deviations observed between the error bars and data points seen in Fig. 18 and the data points seen in Fig. 14.

5. Conclusions

In this work, synchrotron X-ray micro-computed tomography was used to determine the influence of drying air parameters of time, velocity, and temperature on the single pharmaceutical granule drying behaviour of APAP, MCC, LMH, CBZ, and their mixtures. Segmentation was performed to view pore volume changes, with histogram data extracted for the granule region to determine changes in the moisture content. The drying time and sample composition were found to significantly impact the pore volume evolution and the change in moisture ratio for all samples, with parameters of the drying gas velocity and temperature possessing mixed significance on the drying across the range of tested sample compositions. The findings of this work could be used to predict the porosity and moisture content of single granules during the dynamic drying process, with further implications in predicting thermal conductivity and volumetric specific heat capacity for modelling single granule drying within the equations of heat and mass transfer.

Funding information

This research is funded in part by the University of Saskatchewan, and the Natural Sciences and Engineering Research Council of Canada.

CRediT authorship contribution statement

Carter Blocka: Writing – original draft, Visualization, Methodology, Investigation, Conceptualization. **Xiao Fan Ding:** Writing – review & editing, Investigation. **Ning Zhu:** Writing – review & editing,

Investigation. Lifeng Zhang: Writing – review & editing, Supervision, Project administration, Funding acquisition, Conceptualization.

Declaration of competing interest

The authors declare that they have no known competing financial interests or personal relationships that could have appeared to influence the work reported in this paper.

Data availability

Data will be made available on request.

Acknowledgements

The authors would like to gratefully acknowledge Divyapratim Das, Tolu Emiola-Sadiq, Mojtaba Nabipoor Hassankiadeh, Denis Kalugin, and Amy Coller from the University of Saskatchewan for all of their help in performing experiments, who without, this research would not have been possible. The authors would also like to acknowledge Dr. Jerry Heng from the Imperial College of London and Dr. Apostolos Kantzias from the University of Calgary for their technical contributions and recommendations. All research described within this work was performed at the Canadian Light Source, serving the Canadian and global scientific community thanks to the support of the Canada Foundation for Innovation (CFI), the Natural Sciences and Engineering Research Council (NSERC), the National Research Council (NRC), the Canadian Institutes of Health Research (CIHR), the Government of Saskatchewan, and the University of Saskatchewan.

References

- Akpınar, E.K., Toraman, S., 2016. Determination of drying kinetics and convective heat transfer coefficients of ginger slices. *Heat Mass Transf.* 52 (10), 2271–2281.
- Asada, T., Kobiki, M., Ochiai, Y., Iwao, Y., Itai, S., 2017. An innovative method for the preparation of high API-loaded hollow spherical granules for use in controlled-release formulation. *Int. J. Pharm.* 523 (1), 167–175.
- Assar, M., Golmohammadi, M., Rajabi-Hamaneh, M., Hassankiadeh, M.N., 2016. A combined experimental and theoretical approach to study temperature and moisture dynamic characteristics of intermittent paddy rice drying. *Chem. Eng. Commun.* 203 (9), 1242–1250.
- Barakat, N.S., Elbagory, I.M., Almurshed, A.S., 2008. Formulation, release characteristics and bioavailability study of oral monolithic matrix tablets containing carbamazepine. *AAPS PharmSciTech* 9 (3), 931–938.
- Barrett, J.F., Keat, N., 2004. Artifacts in CT: recognition and avoidance. *Radiographics* 24 (6), 1679–1691.
- Bashaiwoldu, A.B., Podczeck, F., Newton, J.M., 2004. A study on the effect of drying techniques on the mechanical properties of pellets and compacted pellets. *Eur. J. Pharm.* 421 (2–3), 119–129.
- Blocka, C., Nabipoor Hassankiadeh, M., Zhang, L., Baik, O.-D., 2023. Effects of moisture content and porosity on the thermal conductivity and volumetric specific heat capacity of pharmaceutical powders. *Int. J. Pharm.* 642, 123130.
- Breinlinger, T., Hashibon, A., Kraft, T., 2015. Simulation of the influence of surface tension on granule morphology during spray drying using a simple capillary force model. *Powder Technol.* 283, 1–8.
- Breinlinger, T., Hashibon, A., Kraft, T., 2015. Simulation of the spray drying of single granules: The correlation between microscopic forces and granule morphology. *J. Am. Ceram. Soc.* 98 (6), 1778–1786.
- Celma, A.R., Cuadros, F., López-Rodríguez, F., 2012. Convective drying characteristics of sludge from treatment plants in tomato processing industries. *Food Bioprod. Process.* 90 (2), 224–234.
- Danalou, S.Z., Ding, X.F., Zhu, N., Emady, H.N., Zhang, L., 2022. 4D study of liquid binder penetration dynamics in pharmaceutical powders using synchrotron X-ray micro computed tomography. *Int. J. Pharm.* 627, 122192.
- Deck, L.-T., Ochsenebein, D.R., Mazzotti, M., 2022. Stochastic shelf-scale modeling framework for the freezing stage in freeze-drying processes. *Int. J. Pharm.* 613, 121276.
- Ding, X.F., Zeinali Danalou, S., Zhang, L., Zhu, N., 2023. In situ wet pharmaceutical granulation captured using synchrotron radiation based dynamic micro-CT. *J. Synchrotron Radiat.* 30 (2), 430–439.
- Faragó, T., Gasilov, S., Emslie, I., Zuber, M., Helfen, L., Vogelgesang, M., Baumbach, T., 2022. Tofu: a fast, versatile and user-friendly image processing toolkit for computed tomography. *J. Synchrotron Radiat.* 29 (3), 916–927.
- Gilpin, R.K., Zhou, W., 2004. Studies of the thermal degradation of acetaminophen using a conventional HPLC approach and electrospray ionization-mass spectrometry. *J. Chromatogr. Sci.* 42 (1), 15–20.
- Groenewold, C., Möser, C., Groenewold, H., Tsotsas, E., 2002. Determination of single-particle drying kinetics in an acoustic levitator. *Chem. Eng. J.* 86 (1), 217–222.
- Grote, S., Kleinebudde, P., 2018. Roll compaction/dry granulation of dibasic calcium phosphate anhydrous—does the morphology of the raw material influence the tabletability of dry granules? *J. Pharm. Sci.* 107 (4), 1104–1111.
- Hamamoto, S., Ohko, Y., Otake, Y., Moldrup, P., Nishimura, T., 2022. Water- and air-filled pore networks and transport parameters under drying and wetting processes. *Vadose Zone J.* 21 (4), n/a.
- He, C., Wang, H., Yang, Y., Huang, Y., Zhang, X., Arowo, M., Ye, J., Zhang, N., Xiao, M., 2021. Drying behavior and kinetics of drying process of plant-based enteric hard capsules. *Pharmaceutics* 13 (3), 335.
- Janocha, M., Tsotsas, E., 2022. Coating layer formation from deposited droplets: A comparison of nanofluid, microfluid and solution. *Powder Technol.* 399, 117202.
- Kan, N.H., Watano, S., 2018. Effect of collision angle on particle-particle adhesion of colliding particles through liquid droplet. *Adv. Powder Technol.* 29 (6), 1317–1322. <https://doi.org/10.1016/j.apt.2018.02.026>.
- Keklikoglou, K., Arvanitidis, C., Chatzigeorgiou, G., Chatzinikolaou, E., Karagiannidis, E., Koletsas, T., Magoulas, A., Makris, K., Mavrothalassitis, G., Papanagnou, E.-D., Papazoglou, A.S., Pavloudi, C., Trougakos, I.P., Vasileiadou, K., Vogiatzi, A., 2021. Micro-CT for biological and biomedical studies: A comparison of imaging techniques. *J. Imag.* 7 (9), 172.
- Kelkar, S., Boushey, C.J., Okos, M., 2015. A method to determine the density of foods using X-ray imaging. *J. Food Eng.* 159, 36–41.
- Khoo, J.Y., Heng, J.Y.Y., Williams, D.R., 2010. Agglomeration effects on the drying and dehydration stability of pharmaceutical acicular hydrate: carbamazepine dihydrate. *Ind. Eng. Chem. Res.* 49 (1), 422–427.
- Kirz, J., Attwood, D. T., Henke, B. L., Howells, M. R., Kennedy, K. D., Kim, K.-J., Kortright, J. B., Perera, R. C. C., Pianetta, P., Riordan, J. C., Scofield, J. H., Stradling, G. L., Thompson, A. C., Underwood, J. H., Vaughan, D., Williams, G. P., & Winick, H. (1986). Center for X-ray Optics, X-ray Data Booklet.
- Kytä, K.M., Lakio, S., Wikström, H., Sulemanji, A., Fransson, M., Ketolainen, J., Tajarobi, P., 2020. Comparison between twin-screw and high-shear granulation - The effect of filler and active pharmaceutical ingredient on the granule and tablet properties. *Powder Technol.* 376, 187–198.
- Lehmann, S., Oesau, T., Jongsma, A., Innings, F., Heinrich, S., 2020. Material specific drying kinetics in fluidized bed drying under mechanical vibration using the reaction engineering approach. *Adv. Powder Technol.* 31 (12), 4699–4713.
- Lesov, I., Tcholakova, S., Denkov, N., 2014. Drying of particle-loaded foams for production of porous materials: mechanism and theoretical modeling. *RSC Adv.* 4 (2), 811–823.
- Li, X., Zhao, Y., Zhao, C., 2021. Applications of capillary action in drug delivery. *iScience* 24 (7), 102810. <https://doi.org/10.1016/j.isci.2021.102810>. PMID: 34296074; PMCID: PMC8282986.
- Li, C., Zhu, N., Emady, H.N., Zhang, L., 2019. Synchrotron-based X-ray in-situ imaging techniques for advancing the understanding of pharmaceutical granulation. *Int. J. Pharm.* 572, 118797.
- Li, C., Zhang, Y., Zhu, N., Emady, H.N., Zhang, L., 2021. Experimental investigation of wet pharmaceutical granulation using in-situ synchrotron X-ray imaging. *Powder Technol.* 378, 65–75.
- Li, C., Blocka, C., Zhang, L., 2022. Experimental investigation on drying performance of pharmaceutical granules in a pulsation-assisted fluidized bed dryer. *Can. J. Chem. Eng.* 100 (9), 2608–2622.
- Maswal, M., Pandith, A.H., Islam, N., Dar, A.A., 2013. Co-solubilization of the hydrophobic drugs carbamazepine and nifedipine in aqueous nonionic surfactant media. *J. Solution Chem.* 42 (7), 1374–1392.
- Maxwell, J.C. (1890). In: Niven, W.D. (ed.). Collected scientific papers. Cambridge University Press, Cambridge. <http://strangebeautiful.com/other-texts/maxwell-scientific-papers-vol-1.pdf>.
- Mayerhöfer, T.G., Pahlow, S., Popp, J., 2020. The bouguer-beer-lambert law: shining light on the obscure. *ChemPhysChem* 21 (18), 2029–2046.
- Mezhericher, M., Levy, A., Borde, I., 2007. Theoretical drying model of single droplets containing insoluble or dissolved solids. *Drying Technol.* 25 (6), 1025–1032. <https://doi.org/10.1080/07373930701394902>.
- Mortier, S.T.F., De Beer, T., Gernaey, K.V., Vercruyse, J., Fonteyne, M., Remon, J.P., Vervaeke, C., Nopens, I., 2012. Mechanistic modelling of the drying behaviour of single pharmaceutical granules. *Eur. J. Pharm. Biopharm.* 80 (3), 682–689. <https://doi.org/10.1016/j.ejpb.2011.12.010>.
- Prakash, B., Pan, Z., 2012. Effect of geometry of rice kernels on drying modeling results. *Drying Technol.* 30 (8), 801–807.
- Putra, R.N., Ajiwiguna, T.A., 2017. Influence of air temperature and velocity for drying process. *Procedia Eng.* 170, 516–519.
- Rantalainen, T., Chivers, P., Beck, B.R., Robertson, S., Hart, N.H., Nimphius, S., Weeks, B. K., McIntyre, F., Hands, B., Siafarikas, A., 2018. Please don't move—evaluating motion artifact from peripheral quantitative computed tomography scans using textural features. *J. Clin. Densitom.* 21 (2), 260–268.
- Reyer, S., Awiszus, S., Meissner, K., Müller, J., 2020. High precision laboratory dryer for thin layer and bulk drying with adjustable temperature, relative humidity and velocity of the drying air. *HardwareX* 8, e00133.
- Sacilik, K., Elicin, A.K., 2006. The thin layer drying characteristics of organic apple slices. *J. Food Eng.* 73 (3), 281–289.
- Said, B.H.L., Najja, H., Farhat, A., Neffati, M., Bellagha, S., 2015. Thin layer convective air drying of wild edible plant (*Allium roseum*) leaves: experimental kinetics, modeling and quality. *J. Food Sci. Technol.* 52 (6), 3739–3749.

- Salager, S., ElYousoufi, M.S., Saix, C., 2010. Effect of temperature on water retention phenomena in deformable soils: theoretical and experimental aspects. *Eur. J. Soil Sci.* 61 (1), 97–107.
- Salmon, A., Hounslow, M. J., Seville, J. P. K., & ScienceDirect, vendor. (2007). Granulation (1st ed., Handbook of powder technology ; v. 11).
- Schiffter, H., Lee, G., 2007. Single-droplet evaporation kinetics and particle formation in an acoustic levitator. Part 1: Evaporation of Water microdroplets assessed using boundary-layer and acoustic levitation theories. *J. Pharm. Sci* 96 (9), 2274–2283.
- Seo, D., Tomizato, F., Toda, H., Uesugi, K., Takeuchi, A., Suzuki, Y., Kobayashi, M., 2012. Spatial resolution of synchrotron x-ray micromotography in high energy range: Effect of x-ray energy and sample-to-detector distance. *Appl. Phys. Lett.* 101 (26), 1.
- Silva, A.F., Sarraguça, M.C., Fonteyne, M., Vercruyse, J., De Leersnyder, F., Vanhoorne, V., Bostijn, N., Verstraeten, M., Vervaet, C., Remon, J.P., De Beer, T., Lopes, J.A., 2017. Multivariate statistical process control of a continuous pharmaceutical twin-screw granulation and fluid bed drying process. *Int. J. Pharm.* 528 (1–2), 242–252.
- Susarla, R., Sievens-Figueroa, L., Bhakay, A., Shen, Y., Jerez-Rozo, J.I., Engen, W., Davé, R.N., 2013. Fast drying of biocompatible polymer films loaded with poorly water-soluble drug nano-particles via low temperature forced convection. *Int. J. Pharm.* 455 (1–2), 93–103.
- Taghavivand, M., Choi, K., Zhang, L., 2017. Investigation on drying kinetics and tribocharging behaviour of pharmaceutical granules in a fluidized bed dryer. *Powder Technol.* 316, 171–180.
- Thomik, M., Gruber, S., Kaestner, A., Foerst, P., Tsotsas, E., Vorhauer-Hugel, N., 2022. Experimental study of the impact of pore structure on drying kinetics and sublimation front patterns. *Pharmaceutics* 14 (8), 1538.
- Triche, B.L., Nelson, J.r., John, T., McGill, N.S., Porter, K.K., Sanyal, R., Tessler, F.N., McConathy, J.E., Gauntt, D.M., Yester, M.V., Singh, S.P., 2019. Recognizing and Minimizing Artifacts at CT, MRI, US, and Molecular Imaging. *Radiographics* 39 (4), 1017–1018.
- Vandeputte, T., Ghijs, M., Van Hauwermeiren, D., Dos Santos Schultz, E., Schäfer, E., Stauffer, F., De Beer, T., Nopens, I., 2023. Mechanistic modeling of semicontinuous fluidized bed drying of pharmaceutical granules by incorporating single particle and bulk drying kinetics. *Int. J. Pharm.* 646, 123447.
- Vandeputte, T., Ghijs, M., De Beer, T., Nopens, I., 2024. Cracking the code: Spatial heterogeneity as the missing piece for modeling granular fluidized bed drying. *Int. J. Pharm.* 657, 124135.
- Vogelgesang, M., Farago, T., Morgeneyer, T.F., Helfen, L., dos Santos Rolo, T., Myagotin, A., Baumbach, T., 2016. Real-time image-content-based beamline control for smart 4D X-ray imaging. *J. Synchrotron Radiat.* 23 (5), 1254–1263.
- Yadav, D., Kumar, N., 2014. Nanonization of curcumin by antisolvent precipitation: Process development, characterization, freeze drying and stability performance. *Int. J. Pharm.* 477 (1–2), 564–577.
- Zammouri, A., Mihoubi, N.B., Kechaou, N., 2022. A performance analysis of batch fluidized bed drying of two pharmaceutical powders by desirability approach. *Drying Technol.* 40 (6), 1210–1231.
- Zeinali Danalou, S., Blocka, C., Yang, J., Zhu, N., Emady, H.N., Wasan, E., Zhang, L., 2023. Advanced 3D and 4D microstructure study of single granule formation for pharmaceutical powders using synchrotron x-ray imaging. *AIChE J.* 69 (5).
- Zhang, Y., Hirpara, V., Patel, V., Li, C., Anderson, R., Zhu, N., Zhang, L., 2021. Imaging of desaturation of the frozen gas diffusion layers by synchrotron X-ray radiography. *Int. J. Hydrogen Energy* 46 (34), 17897–17908.